MASTER

SCIENCE
APPLICATIONS
INCORPORATED

DISTRIBUTION OF THIS DOCUMENT IS UNLIMITED

DISCLAIMER

This report was prepared as an account of work sponsored by an agency of the United States Government. Neither the United States Government nor any agency Thereof, nor any of their employees, makes any warranty, express or implied, or assumes any legal liability or responsibility for the accuracy, completeness, or usefulness of any information, apparatus, product, or process disclosed, or represents that its use would not infringe privately owned rights. Reference herein to any specific commercial product, process, or service by trade name, trademark, manufacturer, or otherwise does not necessarily constitute or imply its endorsement, recommendation, or favoring by the United States Government or any agency thereof. The views and opinions of authors expressed herein do not necessarily state or reflect those of the United States Government or any agency thereof.

DISCLAIMER

Portions of this document may be illegible in electronic image products. Images are produced from the best available original document.

Y/OWI/SUB-77/16519/1

A SIMULATION OF THE THERMOMECHANICAL RESPONSE OF PROJECT SALT VAULT

NOTICE
This report was prepared as an account of work sponsored by the United States Government. Neither the United States nor the United States Energy Research and Development Administration, nor any of their employees, nor any of their contractors, subcontractors, or their employees, makes any warranty, express or implied, or assumes any legal liability or responsibility for the accuracy, completeness or usefulness of any information, apparatus, product or process disclosed, or represents that its use would not infringe privately owned rights.

SAI-FR-702
(Final Report)

Prepared by
Krishan K. Wahi, Donald E. Maxwell, and Ronald Hofmann
Science Applications, Incorporated
8201 Capwell Drive
Oakland, California 94621 950 4156

February 1977

This report was prepared by Science Applications, Incorporated
under Subcontract 86Y-16519V with
Union Carbide Corporation, Nuclear Division,
under Contract Number W-7405-eng-26 with the
Energy Research and Development Administration.
The Subcontract was administered by the Office of Waste Isolation

DISTRIBUTION OF THIS DOCUMENT IS UNLIMITED

Y/OWI/SUB-77/16519/1

A SIMULATION OF THE THERMOMECHANICAL RESPONSE OF PROJECT SALT VAULT

SAI-FR-702
(Final Report)

Prepared by

Krishan K. Wahi, Donald E. Maxwell, and Ronald Hofmann

Science Applications, Incorporated
8201 Capwell Drive
Oakland, California 94621

February 1977

Prepared for

Office of Waste Isolation
Nuclear Division
Union Carbide Corporation
Oak Ridge, Tennessee 37830

NOTICE

This report was prepared as an account of work sponsored by the United States Government. Neither the United States nor the Energy Research and Development Administration, nor any of their employees, nor any of their contractors, subcontractors, or their employees, makes any warranty, express or implied, or assumes any legal liability or responsibility for the accuracy, completeness or usefulness of any information, apparatus, product, or process disclosed, or represents that its use would not infringe privately owned rights.

CONTENTS

		Page
SECTION 1	INTRODUCTION	1
SECTION 2	FORMULATION OF THE PROBLEM	3
	2.1 Background	3
	2.2 Finite-Difference Grid	5
	2.3 Initial and Boundary Conditions	5
	2.4 Idealization of the Heat Sources	8
	2.5 Material Models	9
	2.6 Normalization of the Generalized Creep Model to Lyons Salt	9
	2.7 Heat Losses	13
	2.8 Density Scaling and Dynamic Relaxation	13
SECTION 3	DISCUSSION OF RESULTS	15
	3.1 Room and Pillar Deformations	15
	3.2 Thermal Response	30
	3.3 Sensitivity Analysis	34
SECTION 4	CONCLUSIONS	49
REFERENCES		51
APPENDIX A	CREEP MODELING	52
APPENDIX B	SAMPLE HEATER OUTPUT CALCULATIONS	71
APPENDIX C	DYNAMIC RELAXATION	73

LIST OF FIGURES

		Page
Figure 1a	Plan View of Project Salt Vault Field Test	4
Figure 1b	Finite-Difference Mesh with Boundary Conditions for the First Two Calculations	6
Figure 1c	Finite-Difference Mesh with Boundary Conditions for Sensitivity Calculation	7
Figure 2	Construction of Uniaxial Stress Creep for Lyons Salt at 22.5°C with 4000 psi	12
Figure 3	Initial Grid for the First Two Calculations, Showing the Benchmark and Row and Column Designations	16
Figure 4	Total Heat in the Computational Grid Versus Time	17
Figure 5	Profiles of Grid Top, Roof, Floor, and Grid Bottom at Selected Times, With and Without Creep	18
Figure 6	Computed and Experimental Profiles of the Floor Uplift of the Array Room Measured from Standard Day 806. Center of Array Heaters is Located at 0 Feet	20
Figure 7	Computed Array Room Floor Uplift from Benchmark as a Function of Time, With and Without Creep	21
Figure 8	Computed and Experimental Array Room Roof Sag from Standard Day 806 to 1500	23
Figure 9	Rooms 2 and 3 Floor Uplift Versus Distance from Heated Pillar Wall Starting at Standard Day 1021	24
Figure 10	Room 2 and 3 Pillar Convergence	25
Figure 11	Room 1 and 4 Pillar Convergence	27
Figure 12	Horizontal Deformation Profiles Along Pillar Wall Sections	28
Figure 13	Computed and Experimental Horizontal Deformation of Heated Pillar Walls from Standard Day 806 to 1500	29
Figure 14	Computed and Experimental Horizontal Displacements of Pillar Walls from Standard Day 806 to 1500	31
Figure 15	Vertical Distortions in the Vicinity of Room 3 Computed with Creep and Referenced to Assumed Stationary Point in the Heated Pillar	32
Figure 16	Computed Temperature Contours Around Array Heaters (Day 1353), Pillar Heaters (Day 1500)	33
Figure 17	Temperature History Comparison near Pillar Heater #16	35
Figure 18	Temperature History Comparison near Array Heaters	36

LIST OF FIGURES (continued)

		Page
Figure 19	Temperatures at Day 1500 in the Zones Surrounding Room 3 in the Original Grid (top) and the Sensitivity Grid (bottom)	38
Figure 20	Temperatures at Day 1500 in the Zones Surrounding Room 4 in the Original Grid (top) and the Sensitivity Grid (bottom)	39
Figure 21	Equivalent Stress/$\sqrt{3}$ (Pascals) Versus Time (Days) in the Original Grid in the Middle of Room 3 at a Depth of 2.5 Feet Below the Floor	40
Figure 22	Equivalent Stress/$\sqrt{3}$ (Pascals) Versus Time (Days) in the Sensitivity Grid in the Middle of Room 3 at a Depth of 2.5 Feet Below the Floor	41
Figure 23	Comparisons of Horizontal Profiles at Day 1500 for the Original Grid (dashed) and the Sensitivity Grid (solid). .	42
Figure 24	Comparisons of Vertical Profiles through the Pillar Walls at Day 1500 for the Original Grid (dashed) and the Sensitivity Grid (solid)	44
Figure 25	Room 3 Roof and Floor Contours for Original Grid (dashed) and Sensitivity Grid (solid) at Day 806 and Day 1500 . . .	45
Figure 26	Comparisons of Array Room Floor Uplift and Roof Sag from Day 806 to Day 1500 for Original Grid (dashed), Sensitivity Grid (solid), and Gages (crosses).	46
Figure 27	Comparison of Pillar Wall Horizontal Displacements from Day 806 to Day 1500 for Original Grid (dashed), Sensitivity Grid (solid), and Experiment (crosses)	47

SECTION 1
INTRODUCTION

The feasibility of economically and accurately applying Lagrangian explicit finite-difference (EFD) techniques to the analysis of the thermomechanical response of radioactive wastes placed in salt repositories is demonstrated by the work described in this report. Three numerical simulations of the Project Salt Vault (PSV) experiment (References 1 and 2) were carried out, using STEALTH* 2D (Reference 3), a two-dimensional EFD code. One calculation did not include a model for creep, while the other two calculations used a general model in which creep was included. As expected, when creep was included, it resulted in significantly more pillar shortening and room convergence than when it was not included. The first of the creep simulations (as well as the non-creep simulation) was designed to demonstrate the applicability of the EFD method. The second creep simulation was performed to evaluate the sensitivity of certain numerical parameters, such as zone size and boundary nearness.

The development of a sophisticated model for creep (see Appendix A) capable of being calibrated by data from a laboratory experiment was one of the major accomplishments in this contract. In particular, for the simulations that were performed, the parameters of the creep model were based on data obtained from laboratory pillar experiments performed for Project Salt Vault. These data were surprisingly useful.

Numerical data are presented that compare the results of the three simulations to the results of the Project Salt Vault experiment. In the simulations which included creep, the room closure data are in excellent agreement with the shape and magnitude of the experimentally measured floor and roof closures. Temperature histories were also compared at several locations and these data were also in agreement with the experimental values.

---

*Solids and Thermal hydraulics code for EPRI Adapted from Lagrange TOODY and HEMP. Developed for Electric Power Research Institute by Science Applications, Inc. under Contract RP-307.

Further refinement of the creep model can be achieved by further calibrating creep parameters to different laboratory experiments now underway at Sandia Laboratories, Albuquerque (SLA) and Lawrence Livermore Laboratory (LLL). Additional optimization studies involving zone size, density scaling parameters, etc., can improve accuracy and efficiency. However, the results presented in this report leave no doubt that explicit finite-difference techniques can be used to efficiently calculate the long-term thermomechanical response of salt repositories.

This report contains a description of the simulations performed (Section 2), and a discussion of the computed results (Section 3). Conclusions are presented in Section 4. Details of the material model and numerical equations are located in Appendixes A, B, and C.

SECTION 2
FORMULATION OF THE PROBLEM

2.1 BACKGROUND

Project Salt Vault was a feasibility study of radioactive waste disposal in an underground salt formation. It included a large-scale experiment performed in an inactive salt mine at Lyons, Kansas. For the experiment, a new mining level consisting of five rooms was excavated at about 1000 ft (304.8 m) depth and approximately 15 ft (4.57 m) above an existing level (Figure 1a). Heat sources were arranged and activated so that the imposed heating was essentially symmetric about vertical plane A-A in Figure 1a. Rooms 1 and 4 each contained a circular array of heaters in the middle of their respective rooms. The array heaters were activated on day 1, boosted in power after 434 days (62 weeks), and turned off 142 days (20 weeks) later. Rooms 2 and 3 contained a row of heaters along the central pillar which were turned on twelve months after the array heaters, and were left on for the remaining eleven months of the experiment.

It is possible to consider the entire salt mass and other rock media surrounding the mine in defining the geometry for the EFD simulation if "displacement discontinuity" (DD) models are attached to the EFD boundaries. However, for demonstration purposes, this was not thought to be necessary. Approximations can be made in choosing the locations of the boundaries and the associated boundary values in order to simulate the far-field.* Other possibly more important approximations were made because the simulations were performed using two-dimensional symmetry. In particular, the heat sources were idealized to be compatible with the two-dimensional formulation of a three-dimensional problem. Furthermore, because the heat loads and geometry were nearly symmetric with respect to the vertical plane separating rooms 2 and 3, only one-half of the region was computed -- the part containing rooms 3 and 4. The selection of the mesh, the boundary conditions, the heat sources, and the material properties are discussed next in some detail.

---

*The sensitivity calculation was used to verify the choice of boundary locations and values.

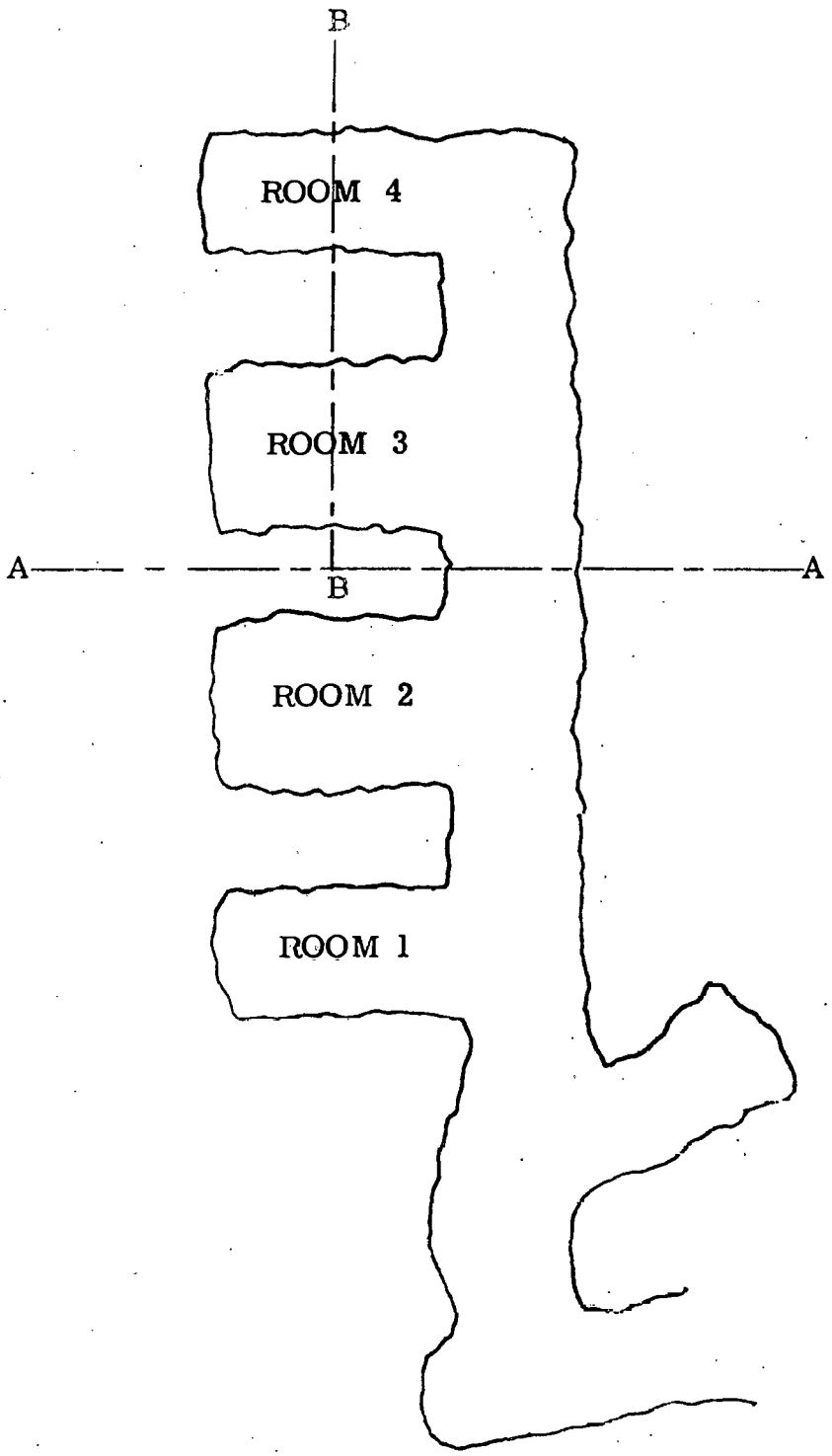

Figure 1a. Plan view of Project Salt Vault field test

2.2 FINITE-DIFFERENCE GRID

A two-dimensional plane-strain geometry was chosen such that the rooms (and pillars) are infinitely long. The cross section (section B-B, Figure 1a) represents a vertical cut through the rooms and the pillars. The overall dimensions of the two-room grid for two of the three simulations are 107.7 ft × 160.0 ft (32.83 m × 48.77 m), as shown in Figure 1b. Room 3 is 40 ft (12.19 m) wide and room 4 is 30 ft (9.14 m) wide. All rooms are 14 ft (4.27 m) high. There are 468 grid points and 425 cells in the mesh. The vertical line (the y-axis) represents the plane of symmetry (section A-A, Figure 1a) so that room 1 and 2 are a mirror image of rooms 4 and 3, respectively. The pillar between rooms 2 and 3 is 20 ft (6.10 m) wide. The pillar between rooms 3 and 4 is 30 ft (9.14 m) wide. The two darkened areas, consisting of 4 cells each, represent the pillar heaters and the array heaters.

The mesh for the sensitivity calculation is shown in Figure 1c. The major mesh differences are (1) the top and bottom horizontal boundaries are farther from the rooms and (2) the pillars each contain one extra zone in the vertical direction.

2.3 INITIAL AND BOUNDARY CONDITIONS

The entire grid, including the rooms, for all three calculations is at an initial ambient temperature of 23°C. The initial state of stress, on the other hand, is not explicitly defined. Instead, an overburden calculation is performed that simulates instantaneous and simultaneous excavation of the rooms, and the stresses and stress concentrations are allowed to develop to their static equilibrium values. For the first two calculations, the boundary stresses on the top and at the bottom of the grid are the overburden stresses for those elevations based on 1 psi/ft of depth below the surface. The floor of the rooms is assumed to be 986 ft (300.5 m) below the ground level. Accordingly, boundary stresses of 937 psi (6.462×10^6 Pa) on top

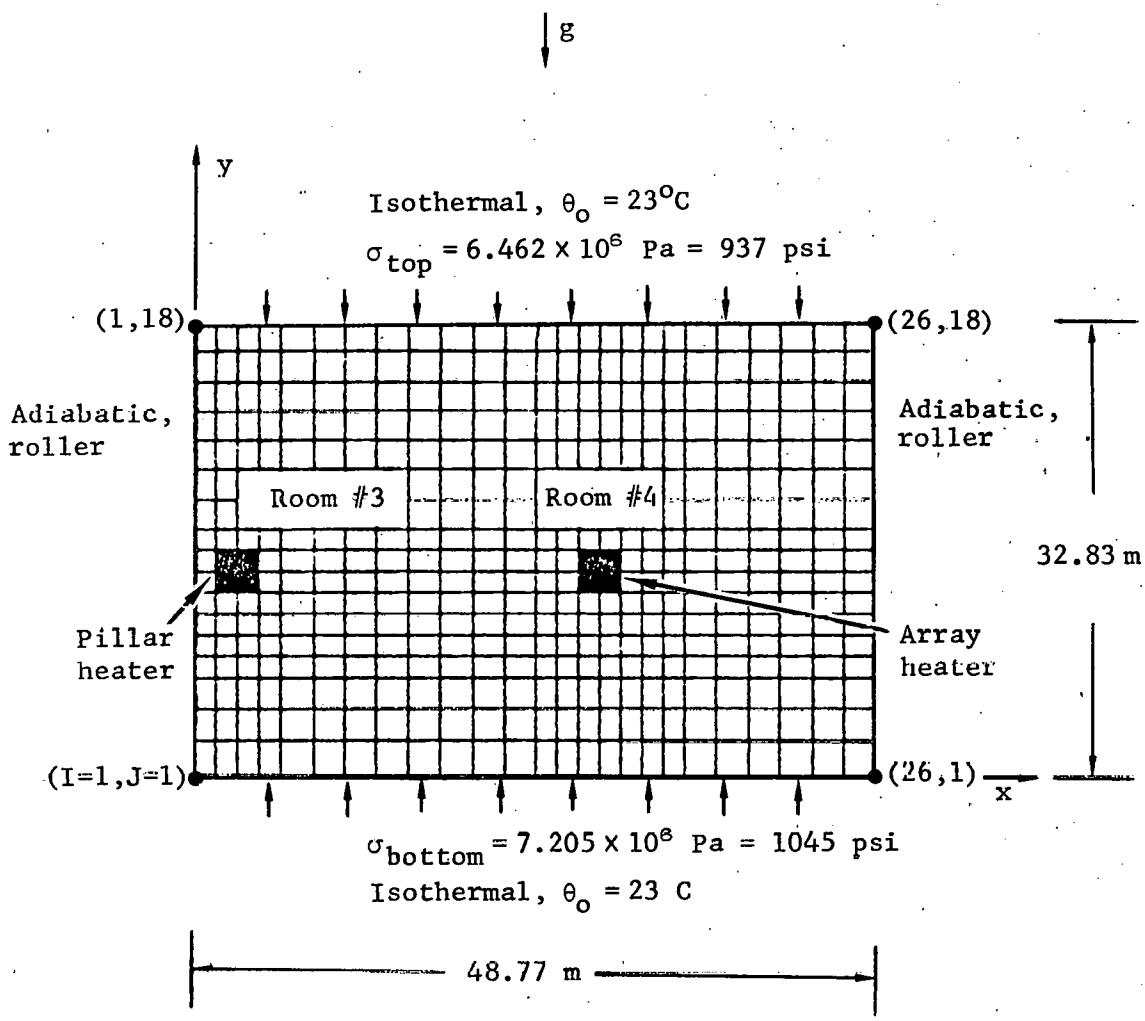

Figure 1b. Finite-difference mesh with boundary conditions for the first two calculations.

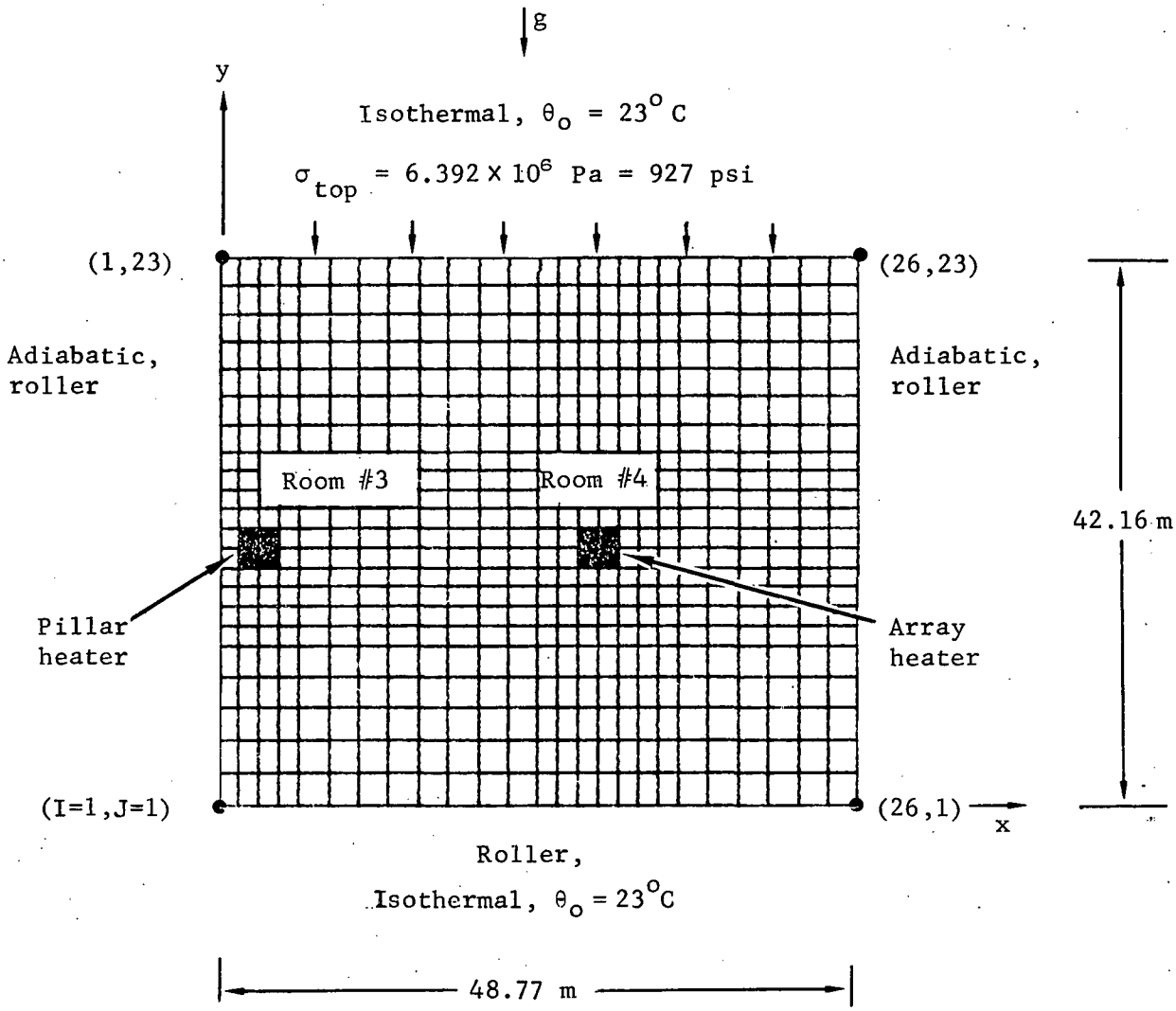

Figure 1c. Finite-difference mesh with boundary conditions for sensitivity calculation.

and 1045 psi (7.205×10^6 Pa) at the bottom are specified. For the grid shown in Figure 1c, the overburden was computed from slightly different top and bottom boundary conditions. The top boundary used a stress based on the ρgh value for a depth, h, of 922 ft (281 m) and an average overburden density of 145 lb/ft^3 (2318 kg/m^3). This led to a stress of 927 psi (6.392×10^6 Pa). The bottom boundary did not use stress, but instead was a vertically rigid and horizontally free roller boundary.

Horizontally rigid (but vertically free) mechanical boundary conditions are assumed for the left and the right edges of both grids. The left boundary condition is an exact representation of a plane of symmetry and the right boundary condition is an idealized approximation of an infinite horizontal extent. The temperature boundary conditions are isothermal on the top and on the bottom, and adiabatic on the left and on the right. The left temperature boundary condition is exact (due to symmetry) and the other three are idealized. For the period of the present simulation (23 months), these are considered to be fairly accurate.

For long-term simulations, say of 30 years, more realistic boundary descriptions are necessary. For example, the total height of the finite-difference grid may have to be increased, or thermally interactive grids on the top and on the bottom may have to be added on. All boundary conditions of the three calculations are summarized in Figures 1b and 1c.

2.4 IDEALIZATION OF THE HEAT SOURCES

The physical size, as well as the geometric arrangement of the pillar heaters and the array heaters, have to be compromised in order to describe them by means of cells in a finite-difference grid. In the experiment, there were 22 pillar heaters buried under the edges of the pillar along the length of the room and the array heaters were arranged in a circular pattern and buried in the center of the room, as described in Reference 1. In the idealized geometry for the finite-difference calculation, pillar heaters,

as well as array heaters, are all represented by infinitely long square prisms. This is considered to be a good approximation of the pillar heaters, since their arrangement is essentially two-dimensional even in the experiment. The power output of the idealized pillar heater is computed by dividing the actual pillar heater output by the spacing between the heaters. The array heater output is a more crude approximation because of the three-dimensional nature of the heater arrangement with respect to the assumed plane strain geometry of the grid. Sample calculations of the pillar and array heater output are given in Appendix B.

2.5 MATERIAL MODELS

The nominal material properties for salt are presented in Table 1. An arbitrary yield limit of 14,500 psi (1.0×10^8 Pa) is specified and salt is assumed to be elastic-perfectly plastic. The creep model is discussed in Appendix A. The sources of these data are also identified in Table 1. A temperature-dependent thermal conductivity model is used. The specific heat capacity is assumed to be a constant.

2.6 NORMALIZATION OF THE GENERALIZED CREEP MODEL TO LYONS SALT

The creep model, represented by Eqs.(A-6a) through (A-6c) in Appendix A, requires input values for the parameters A, a, b, and c. To be consistent with McClain's model (Reference 1), the values selected for a, b, and c were

$$a = 0.3,$$
$$b = 9.5,$$
$$c = 3.0.$$

In McClain's model, the coefficient A applies to circular pillars of Lyons salt with a 4:1 width-to-height ratio ($W/H = 4$) and a size scale of the order of inches. In addition, these pillars had a particular structure adjoining the top and bottom which was an integral part of the experiments. (See Figure A-1 of Appendix A.)

TABLE I. NOMINAL MATERIAL PROPERTIES

Material Property	Numerical Value	Source
Young's modulus, E	6.895×10^9 Pa (1×10^6 psi)	ORNL-4555, p.302
Poisson's ratio, ν	0.4	ORNL-4555, p.302
Mass density, ρ	2161 kg/m^3 (135 lb/ft^3)	ORNL-4789, p.34
Density scaling factor	9.8889×10^{16}	derived*
Bulk modulus, B	1.14917×10^{10} Pa (1.67×10^6 psi)	derived
Shear modulus, G	2.4625×10^9 Pa (3.57×10^6 psi)	derived
Specific heat capacity, C_p	930.97 J/kg $^\circ$K (0.222 Btu/lbm $^\circ$F)	ORNL-4789, p.34
Thermal conductivity, K	$K(\theta)$** in J/(s·m·$^\circ$K)	ORNL-4789, p.33
Linear coefficient of thermal expansion, α	4.0×10^{-5} (m/m)/$^\circ$K [22.2 (μin./in.)/$^\circ$F]	ORNL-4555, p.266
Convective heat transfer coefficient, h_c	5.886 J/(s·m^2·$^\circ$K) [1.04 Btu/(hr·ft^2·$^\circ$F)]	ORNL-4789, p.67

*Chosen such that the stable mechanical time step is one-half to one-fourth of the stable thermal time step.

**$K(\theta) = 6.109 - 2.5148 \times 10^{-2}\theta + 7.153 \times 10^{-6}\theta^2 - 8.293 \times 10^{-8}\theta^3$ where θ is in $^\circ$C.

Conversion factor: 1 J/(s·m·$^\circ$K) = 0.578 Btu/(hr·ft·$^\circ$F)

The generalized creep model, employing stress-strain invariants, requires a generalized value of A which does not depend on the geometry. This value can be determined from uniaxial stress experiments. Since these were not available, the creep data for different width-to-height ratio pillars were extrapolated to $W/H = 0$, corresponding to uniaxial stress. This procedure is described next.

Figure 12.25 of Reference 1 provides laboratory pillar shortening data for the cases W/H = 2, 3, and 4 for Lyon's salt at 22.5°C with an applied load of 4000 psi. These data suggest that the elastic contribution to the pillar strain was about 0.67%, and this value was subtracted from each of the three cases to estimate the creep contribution. The resulting creep strain versus time was converted to natural strain by $e_{xx}^{nat} = \log(1 + \Delta x/x_o)$ where $\Delta x/x_o$ corresponds to the engineering strain. Then e_{xx}^{nat} was converted to the second invariant of strain deviation by assuming

$$e_{yy}^{nat} = e_{zz}^{nat} = -e_{xx}^{nat}/2$$

to arrive at

$$< e^{cr} > = 0.866 \log_e(1 + \Delta x/x_o) .$$

Point values of e_{xx}^{nat} versus time are plotted on log-log scale in the upper diagram of Figure 2 for the three cases, $W/H = 2$, 3, and 4 (temporarily ignoring the case $W/H = 0$). These data points were then smoothed by the indicated straight-line fits corresponding to a $t^{0.3}$ power law. The smoothed data were then re-plotted in the lower diagram of Figure 2 and extrapolated to the case $W/H = 0$, as shown. The resulting $W/H = 0$ data were then plotted in the upper diagram of Figure 2 and smoothed by the $t^{0.3}$ straight-line fit to arrive at the estimated creep response for the uniaxial stress case.

The generalized creep model was then exercised in a subsidiary computer simulation to obtain a fit with the constructed $W/H = 0$ data. The resulting value of A was larger than McClain's value by a factor of 3.5. This new

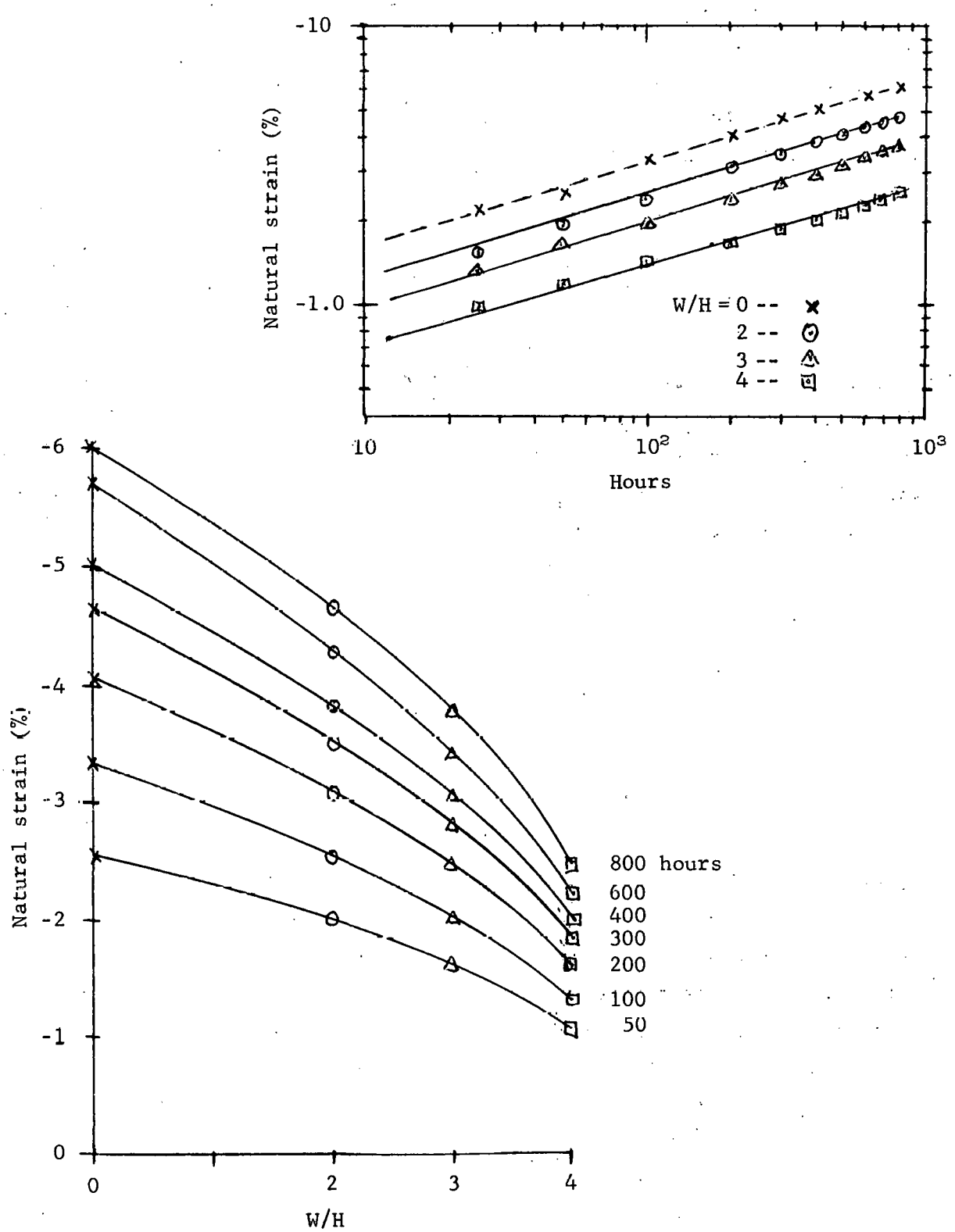

Figure 2. Construction of uniaxial stress creep for Lyons salt at 22.5°C with 4000 psi.

value was then employed in the full-scale simulation of the Lyons mine experiment with no further normalization. The relatively good agreement that was obtained in the subsequent PSV simulations suggests that the size effect is small going from these laboratory experiments to the full-scale Lyons mine.

2.7 HEAT LOSSES

Convection losses at the room walls are estimated by assuming that the rooms are maintained at the ambient temperature of 23°C. Equation (1) gives the heat loss in Joules in an increment of time, Δt, for a cell with a surface area, S,

$$Q_{convection} = -h_c \times (\theta - 23^{\circ}) \times S \times \Delta t \,. \tag{1}$$

In addition, heat is lost through the isothermal boundaries.

2.8 DENSITY SCALING AND DYNAMIC RELAXATION

Although Lagrange explicit finite-difference programs may be used to compute the static equilibrium or the quasi-static response of a system, they can be very expensive in terms of computer costs unless special techniques are employed. In problems of a static or quasi-static nature, the dynamic response due to stress-wave propagation is not important. It is the long-term or steady-state solution that is desired. Fortunately, techniques have been developed that can reduce the calculational time necessary to achieve steady state or equilibrium by compromising the detail (i.e., dynamic response) but <u>without</u> compromising the accuracy of the final solution. These techniques will be referred to collectively as dynamic relaxation techniques. Some background material on dynamic relaxation methods and their successful use in the past is presented in Appendix C.

Because time is an explicit variable, some stability criterion must be used in determining a stable time step. The Courant stability criterion is used for stress-wave propagation, such that $\Delta t \leq (\Delta \ell / c_\ell)_{min}$ where $\Delta \ell$ is a

typical zone dimension and c_ℓ is the sound speed. For diffusion stability, the time step is controlled by the condition that $\Delta t \leq \Delta \ell^2/2\alpha$, where α is the thermal diffusivity. For a given zone size, the thermal time step is generally orders of magnitude larger than the mechanical time step. It is for this reason that special techniques, such as density scaling, are used to make the two time steps similar.

The specific heat is defined on a volumetric basis so that scaling the density does not affect the thermal characteristics of the material. The concept of density scaling is valid for quasi-static problems in which the effects of momentum may be ignored. A density scaling factor of 9.89×10^{16} was chosen, which makes the mechanical time step one-half to one-fourth (depending on temperature and cell dimensions) of the stable thermal time step for this problem. A dynamic relaxation factor that is consistent with the new "system frequency" response must also be chosen. This is generally done by first running the problem without dynamic relaxation for a period long enough to identify the lowest frequency of the system. In STEALTH formulation of the input, the dynamic relaxation factor, ω_o, can be estimated by using the formula,

$$\omega_o = 2\pi/T ,$$

where T is the longest period of oscillation of the system.

SECTION 3
DISCUSSION OF RESULTS

3.1 ROOM AND PILLAR DEFORMATIONS

Figure 3 is a duplicate of the mesh shown in Figure 1b except that it contains row and column numbering data to facilitate a discussion of the output from the first two calculations. The vertical lines labeled Columns 3, 9, 13, and 19 run along the pillar walls. The horizontal lines containing the room floors and roofs are, respectively, Row 11 and Row 13. A benchmark grid point (Column 26, Row 11) was selected as a moving reference with which to measure floor uplift and roof sag. This was necessary because of the substantial time-dependent grid distortion that prevailed over the entire grid.

Figure 4 displays the total heat versus time in the grid and provides a time schedule for changes of input power. Creep was not turned on until standard day 806, after stress equilibrium was computed from hydrostatic overburden boundary conditions following the instantaneous excavation of the rooms.

Figure 5 displays the vertical distortions on a magnified scale for the top and bottom of the grid, and the roof and floor rows of the rooms. A slight point-to-point mesh oscillation is apparent at day 806, which becomes much larger at day 1500 for the case of creep. This "zigzag" effect can be eliminated by the proper application of a technique known as triangle artificial viscosity (Reference 4). The technique was not applied in this simulation. The sensitivity calculation described later showed that the zigzag effect could be reduced significantly by fixing the bottom boundary.

The motion of the benchmark point was different with creep than without creep. The corresponding floor lifts and roof sags were established by employing the appropriate benchmark. It should be noted that the left neighbor

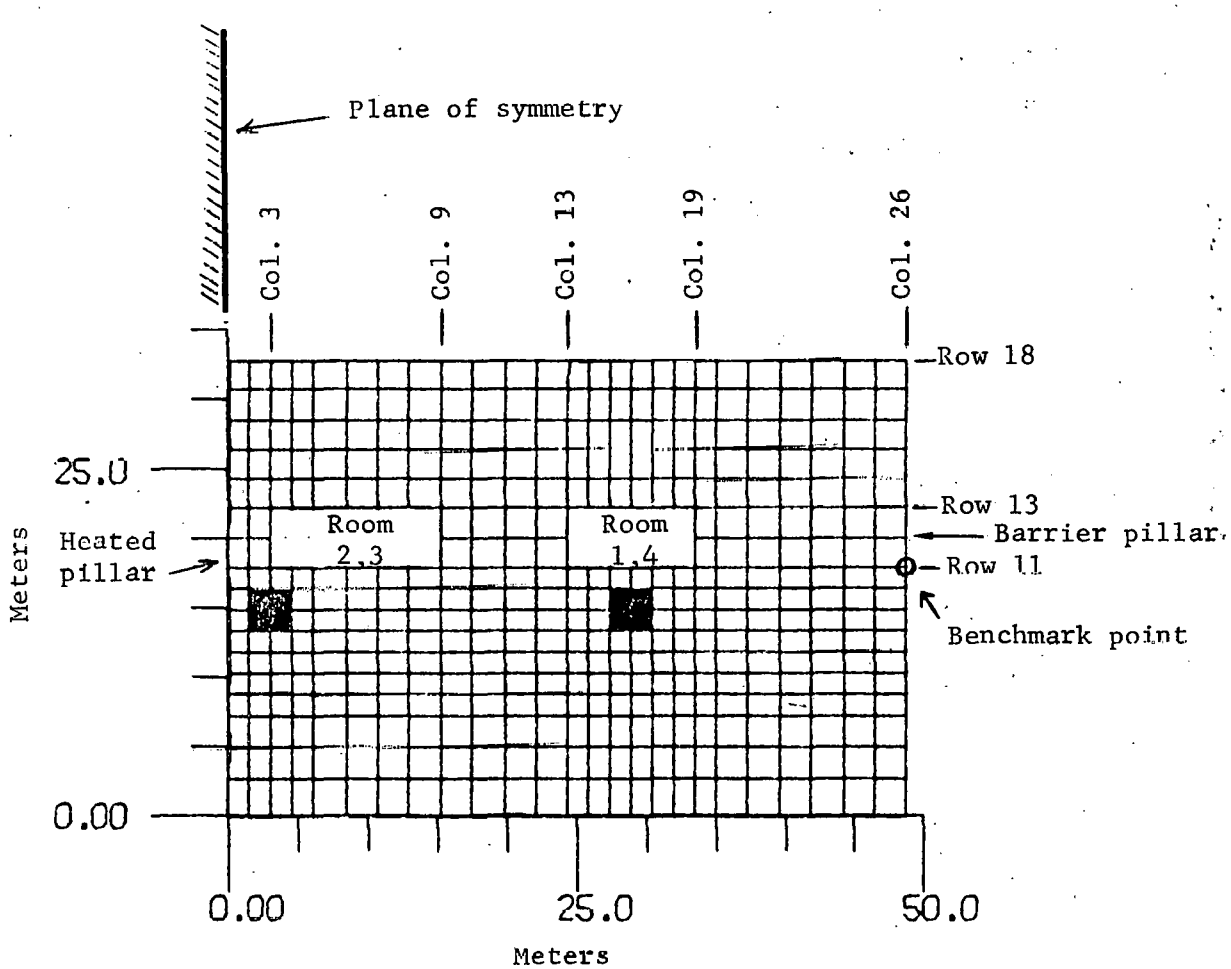

Figure 3. Initial grid for the first two calculations, showing the benchmark and row and column designations.

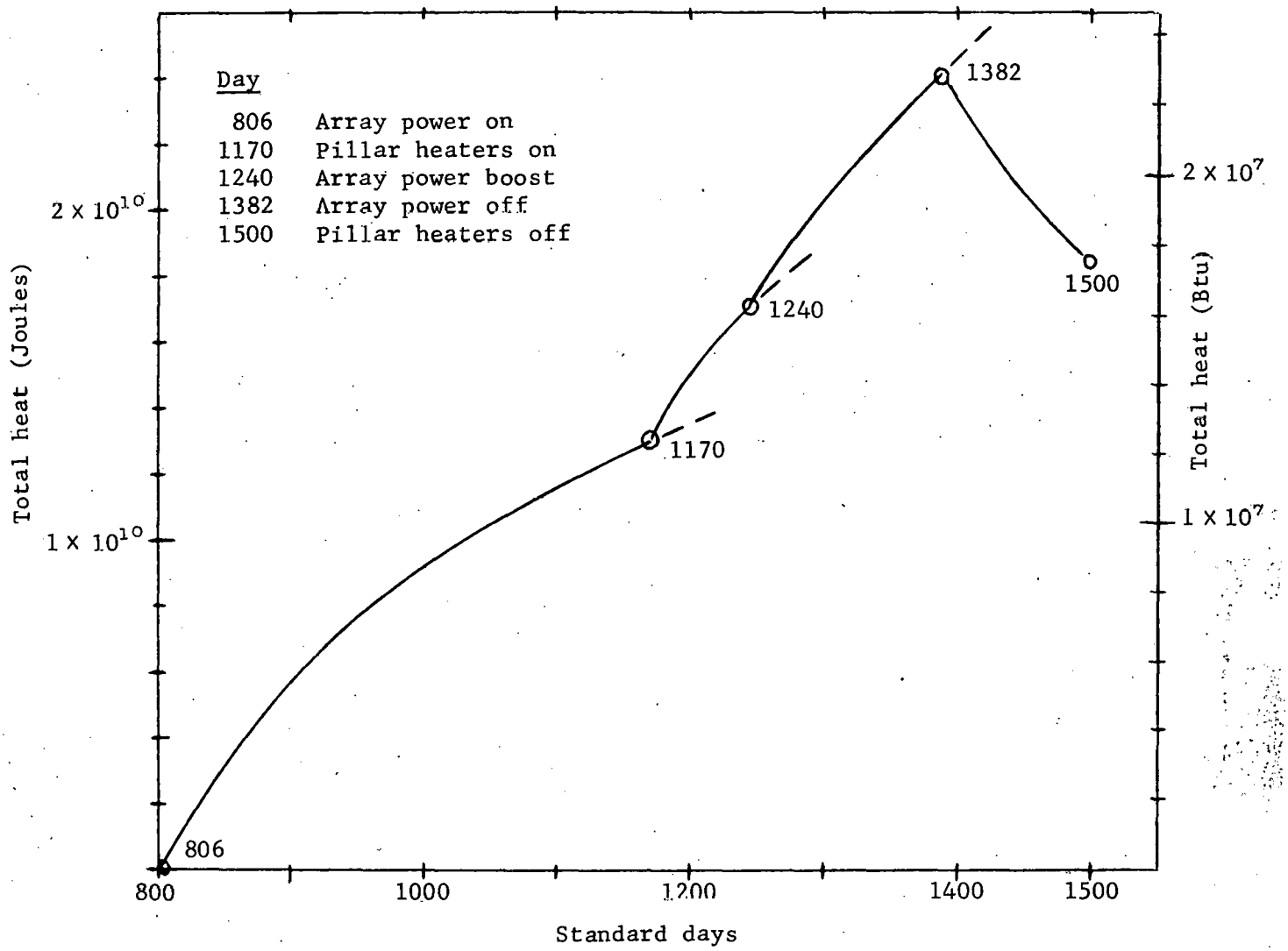

Figure 4. Total heat in the computational grid versus time.

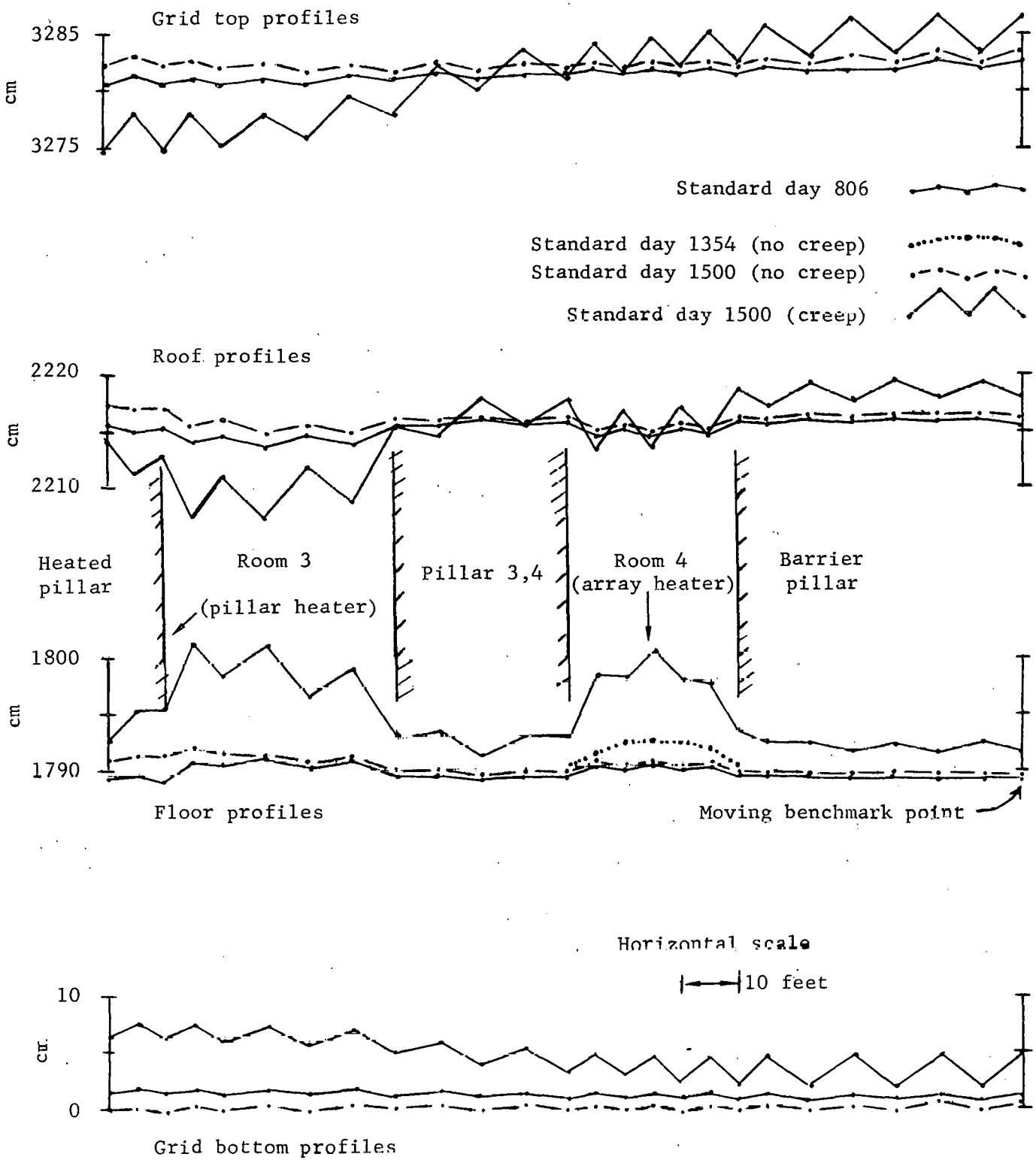

Figure 5. Profiles of grid top, roof, floor, and grid bottom at selected times, with and without creep.

point of the benchmark lifts more than the chosen benchmark. If this neighbor point is used as an alternate benchmark, then the subsequent floor lift at day 1500 with creep will be reduced by about one centimeter, while the roof sag will be increased by this amount. This will be reiterated in the discussion that follows.

Profiles of the array-room floor uplift are displayed and compared to experimental data in Figure 6. The computed results with creep tend to be higher, and are about one centimeter higher at the last time. If the alternate benchmark is used, the agreement is even better. This alternative benchmark will also bring the array-room roof sag into better agreement with the experiment. This will be seen later. However, it must be recalled that the creep model was turned on simultaneously with the array power, with no past history to retard the day 806 creep strain rate. It should also be noted that simulated nominal array-room width is smaller than that of the real array-room, which tends to retard the uplift. Finally, the 2D simulaticn of the 3D geometry cannot be expected to be correct without normalization. Therefore, the computed and experimental comparisons may be fortuitous to some extent.

Figure 7 displays the computed array-room floor uplift versus time for the seven grid points of the floor. The top diagram locates the points of the floor. The middle diagram displays the results without creep, while the lower diagram gives the results with creep on a different vertical scale. The dashed lines in these diagrams indicate where the path details are uncertain because of a lack of intermediate printout data.

It can be noted that the uplift without creep is almost constant from day 900 to 1200, with values A, B, C, and D as indicated. The 1.4 factor power boost then results in an approximate 1.4 factor in the uplift after a time lag. The power-off condition then results in negligible uplift at day 1500. The alternative benchmark point without creep has only a small effect on these results.

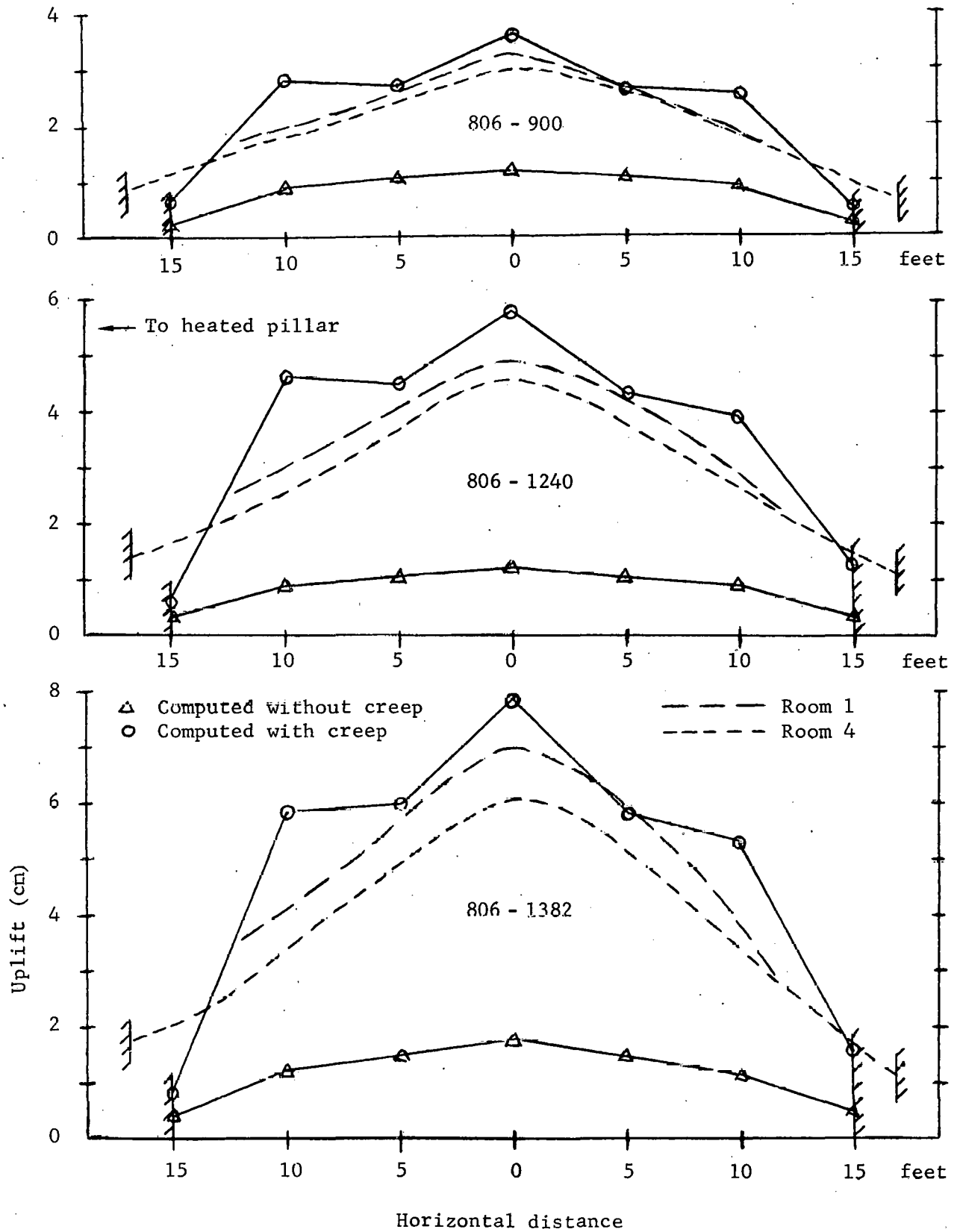

Figure 6. Computed and experimental profiles of the floor uplift of the array room measured from standard day 806. Center of array heaters is located at 0 feet.

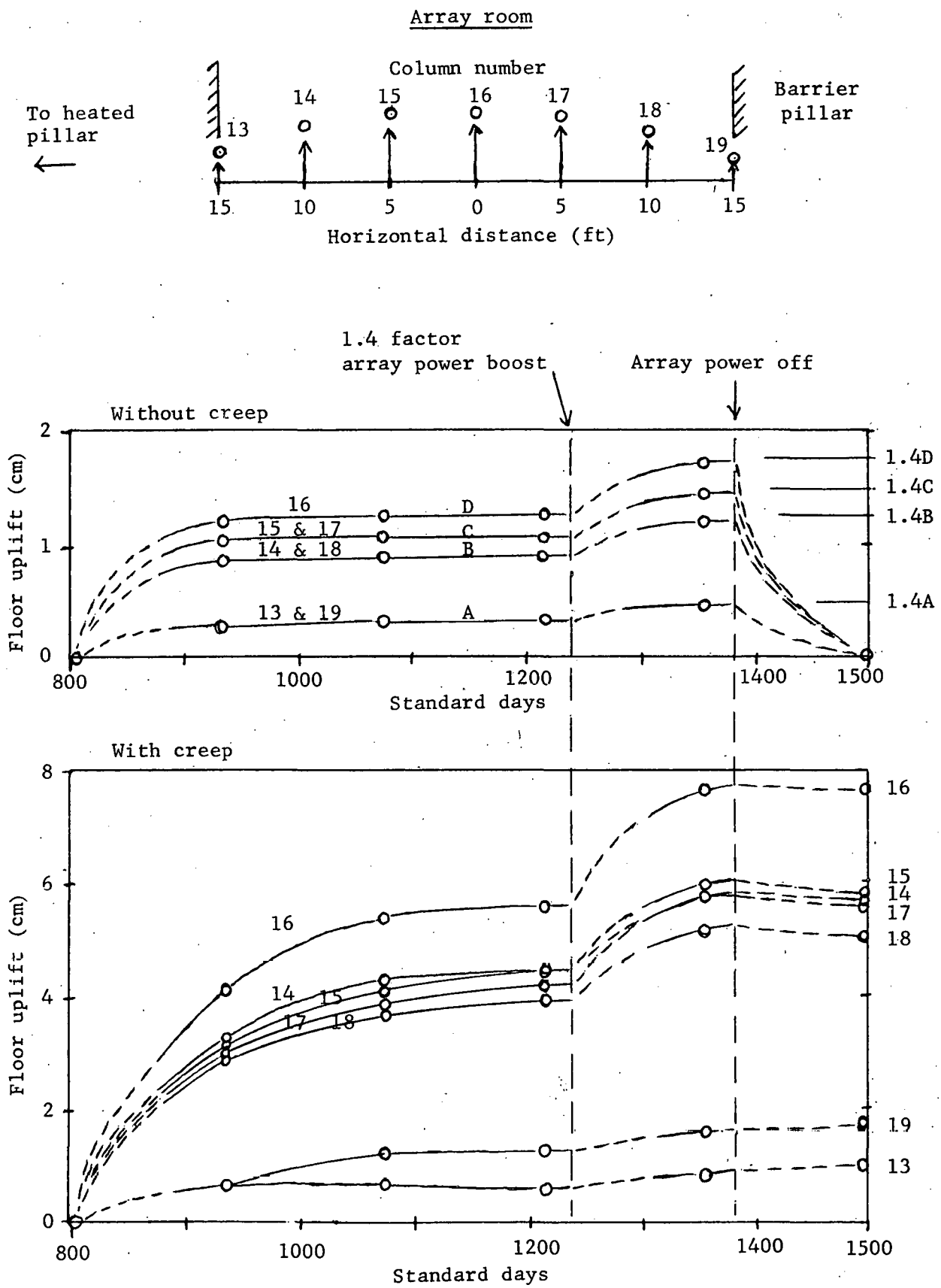

Figure 7. Computed array room floor uplift from benchmark as a function of time, with and without creep. (Note vertical scale difference.)

The uplift with creep has a different character and is about five times as large as that without creep when the array power is on. The slight recovery after the arrays turn off is due to the thermal contraction.

Figure 8 displays the array-room roof sag computed with creep, along with experimental data for the indicated gages. The zigzag character of the computed result is accentuated by the vertical magnification. Nevertheless, it is annoying and should be eliminated in the future by the means mentioned earlier. The one-centimeter downward correction that would apply for the alternative benchmark would bring the computation into excellent average agreement with the experiment. However, previous remarks apply and the agreement may be fortuitous.

Figure 9 displays the computed floor uplift with creep in room 3 (and, by symmetry, in room 2) next to the heated pillar. The 2D simulation of this region should be more accurate than that of the array room because of the heat source geometry. However, the results show computed values that are lower than the experiment when comparing to room center measurements.* The results would be still lower if the alternative benchmark point were employed. This raises the question of the proper 2D benchmark for the true PSV case.

Referring back to Figure 5, it can be noted that the general floor profile through the total grid tends to raise as the heated pillar is approached from the right. Similarly, the roof profile tends to sag even more. The result is that the room 3 roof sag is larger than the floor uplift when either the reference or alternative reference point is used. This is not realistic for the true PSV case and further thought is required to resolve this normalizing problem. Nevertheless, the shape and magnitude of the computed floor uplift must be considered to be satisfactory with respect to demonstrating computational capability.

The pillar convergences of rooms 2 and 3 are compared to the computed results with creep in Figure 10. The upper diagram locates the experimental

---

*Floor uplift measurements taken at the front and back of the room are lower than the comparable measurements made at the room center.

Plan View of Four Rooms

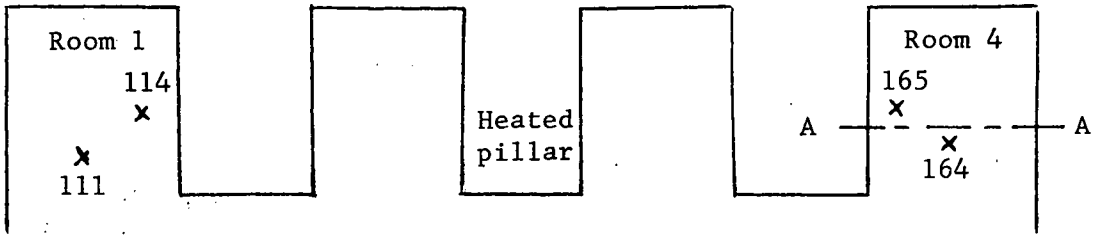

Section A-A

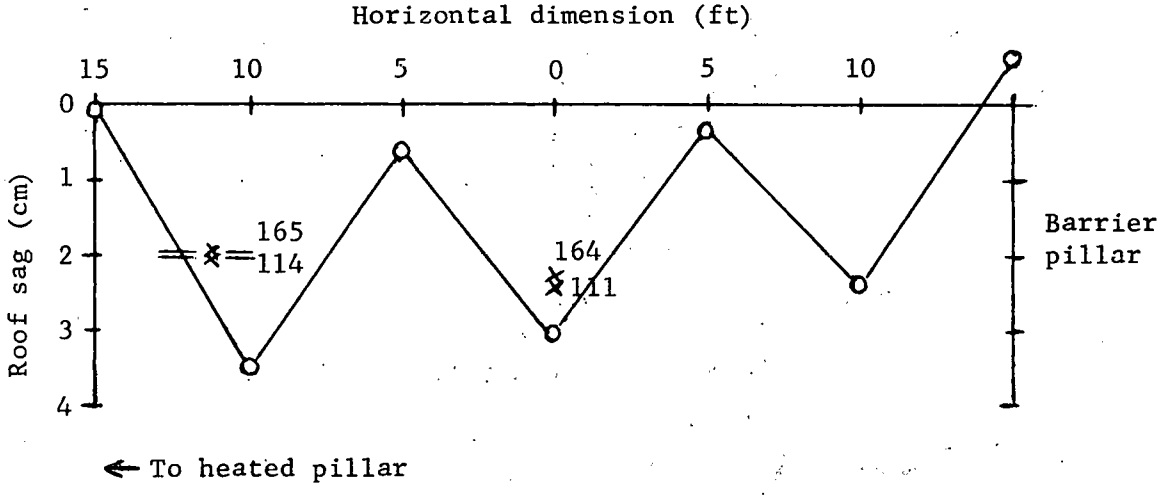

O Computed with creep

X Experimental data, Ref. 1, Figures 11.65, 11.66

Figure 8. Computed and experimental array room roof sag from standard day 806 to 1500.

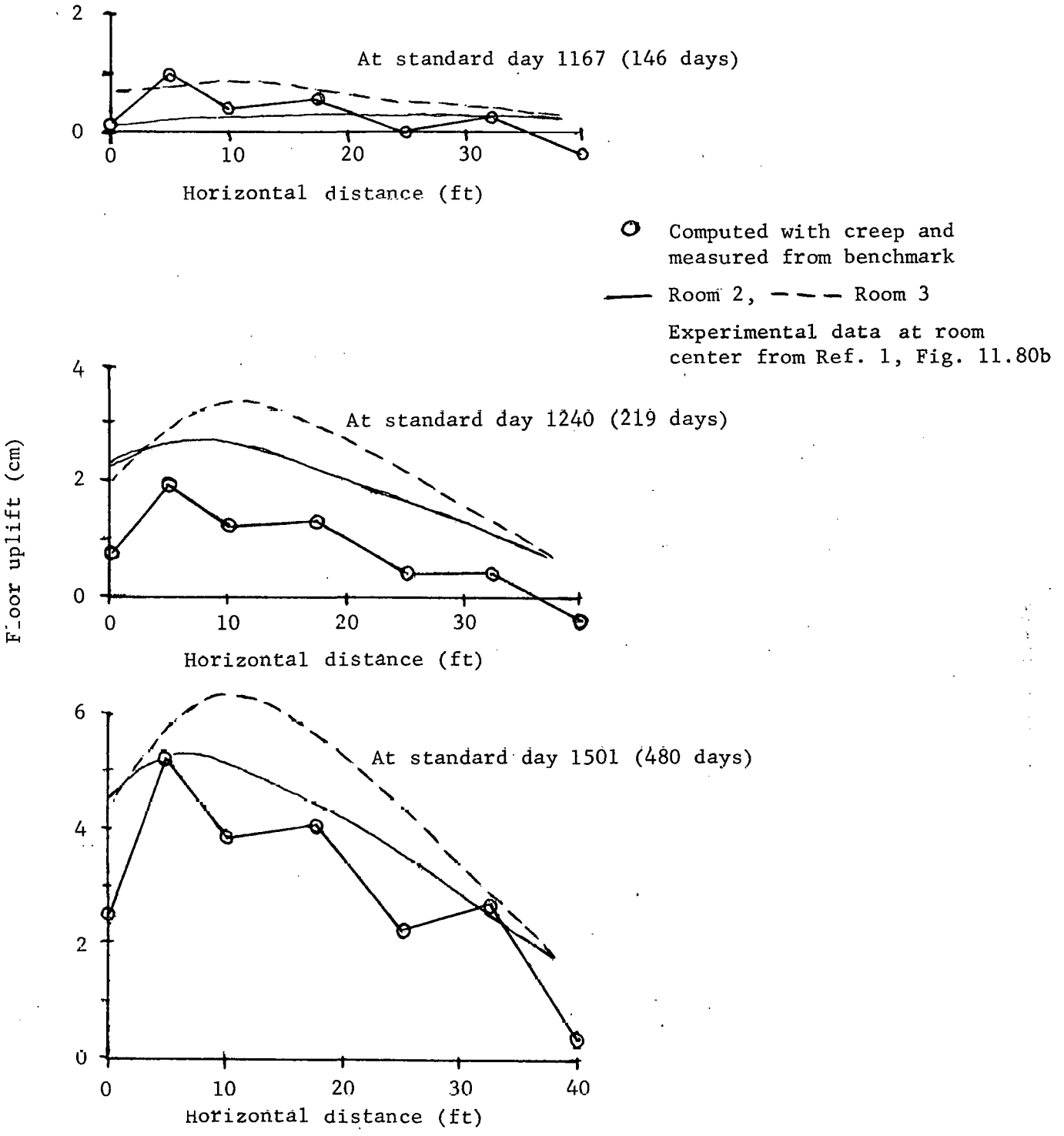

Figure 9. Rooms 2 and 3 floor uplift versus distance from heated pillar wall starting at standard day 1021. Edge of heated pillar is located at 0 feet.

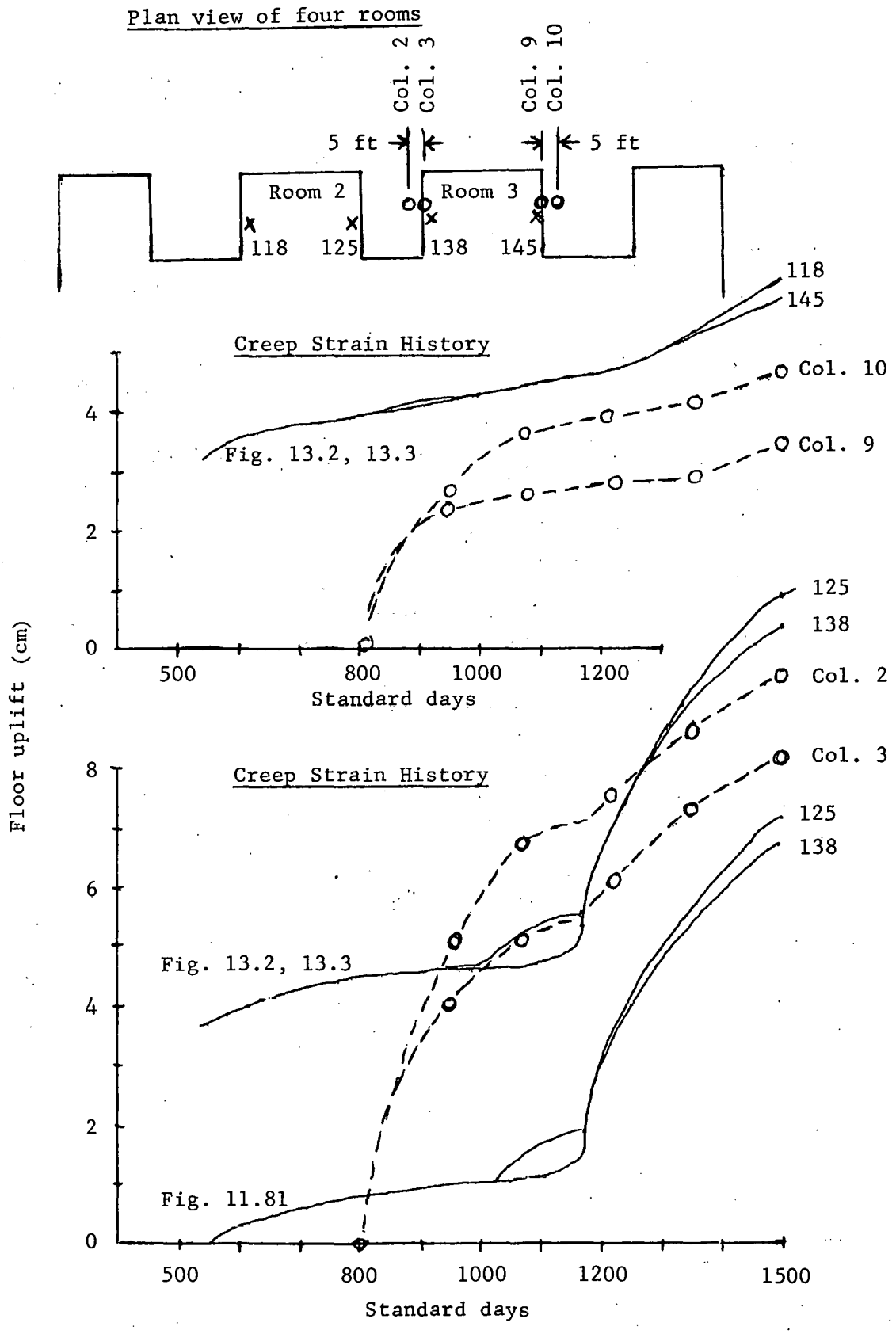

Figure 10. Room 2 and 3 pillar convergence. Experimental data (x and solid lines) from Ref. 1. Computed data with creep (o and dashed lines) at indicated column numbers.

gages and the computational points. Though the magnitude of the results at day 1500 are similar, the time dependencies are different, pointing out the substantial error associated with the computed creep starting abruptly at day 806. The zigzag effect is also pronounced, as can be seen in the comparisons of Columns 2 and 3, and Columns 9 and 10. The lower diagram contains two references to the same gage response. Presumably, the Figure 11.81 data from ORNL-4555 (Reference 1) has a normalized base line rather than an absolute one.

Figure 11 compares room 1 and room 4 pillar convergences to the results computed with creep. The gages and computation points are located in the upper diagram. The computed results in the lower diagram are substantially lower than the experiment, presumably due to the shorter time for creep to accumulate strain in the calculation. The zigzag effect of Columns 12 and 13 is large. Columns 19 and 20 do not show this. This may be due to the observation that Columns 19 and 20 along the floor profile were both buckled downward at a transition of "zigzag" to "zagzig".

Figure 12 displays horizontal deformation on grid columns 3, 9, 13, and 19 along the pillar walls and extending well into the roof and floor. The upper diagram displays standard day 806 and day 1500 with creep. The lower diagram displays the net deformation measured from day 806 for day 1354 and day 1500 without creep, and to day 1500 with creep. It is apparent that the pillar walls do not contain enough computational points for a satisfactory simulation of pillar thickening. The three points defining the entire height of the pillar do not provide even a full cycle of zigzag to allow for a reasonable estimate of pillar average thickening. This must be recalled in evaluating the results that follow.

Figure 13 displays experimental and computational data with and without creep for the thickening of the heated pillar from day 806 to day 1500. The computed result without creep is small. The result with creep is larger than that of the experiment. The discrepancies are not unexpected in view of earlier remarks.

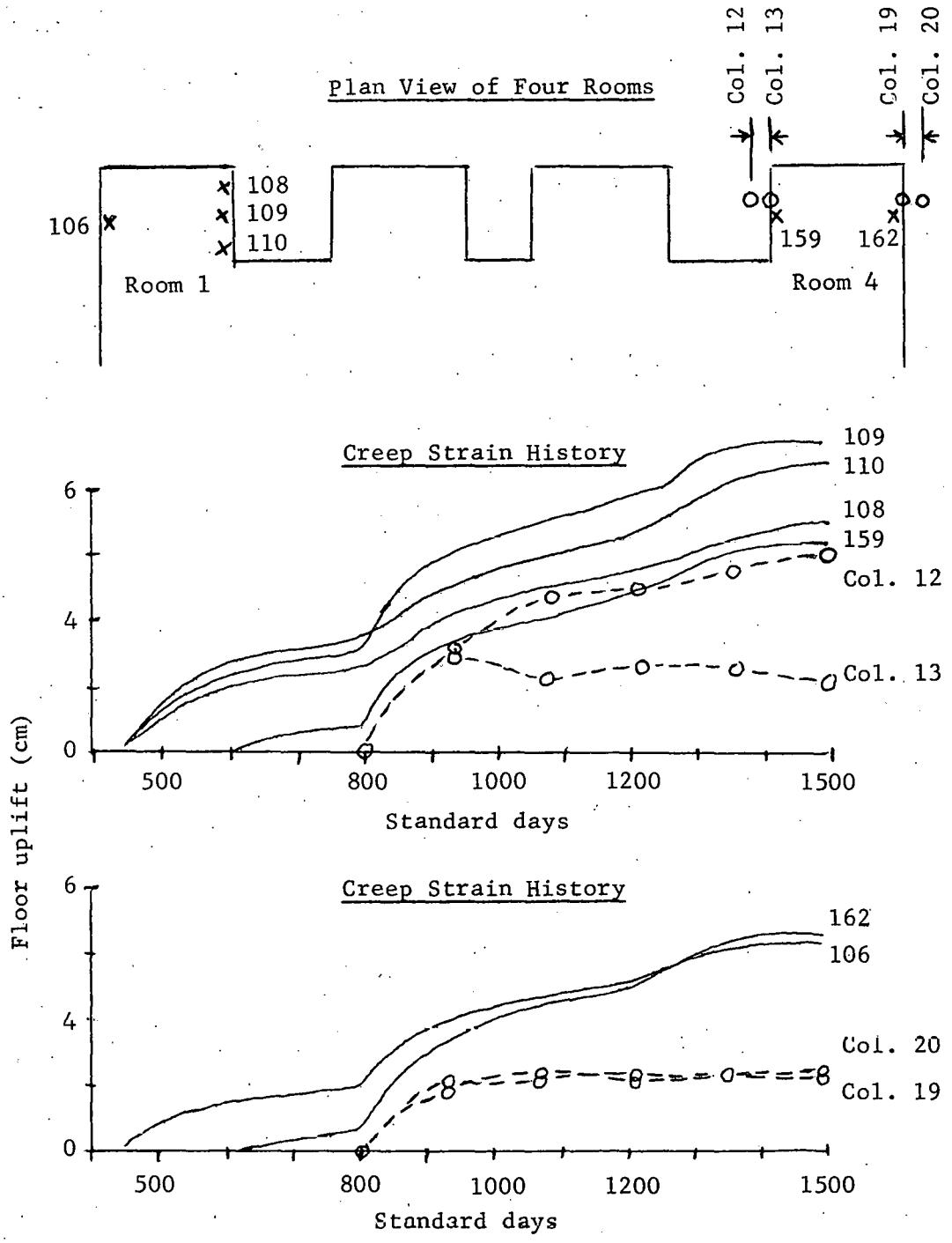

Figure 11. Room 1 and 4 pillar convergence. Experimental data (x and solid lines) from Ref. 1, Figures 11.60a and b. Computed data with creep (o and dashed lines) at indicated column numbers.

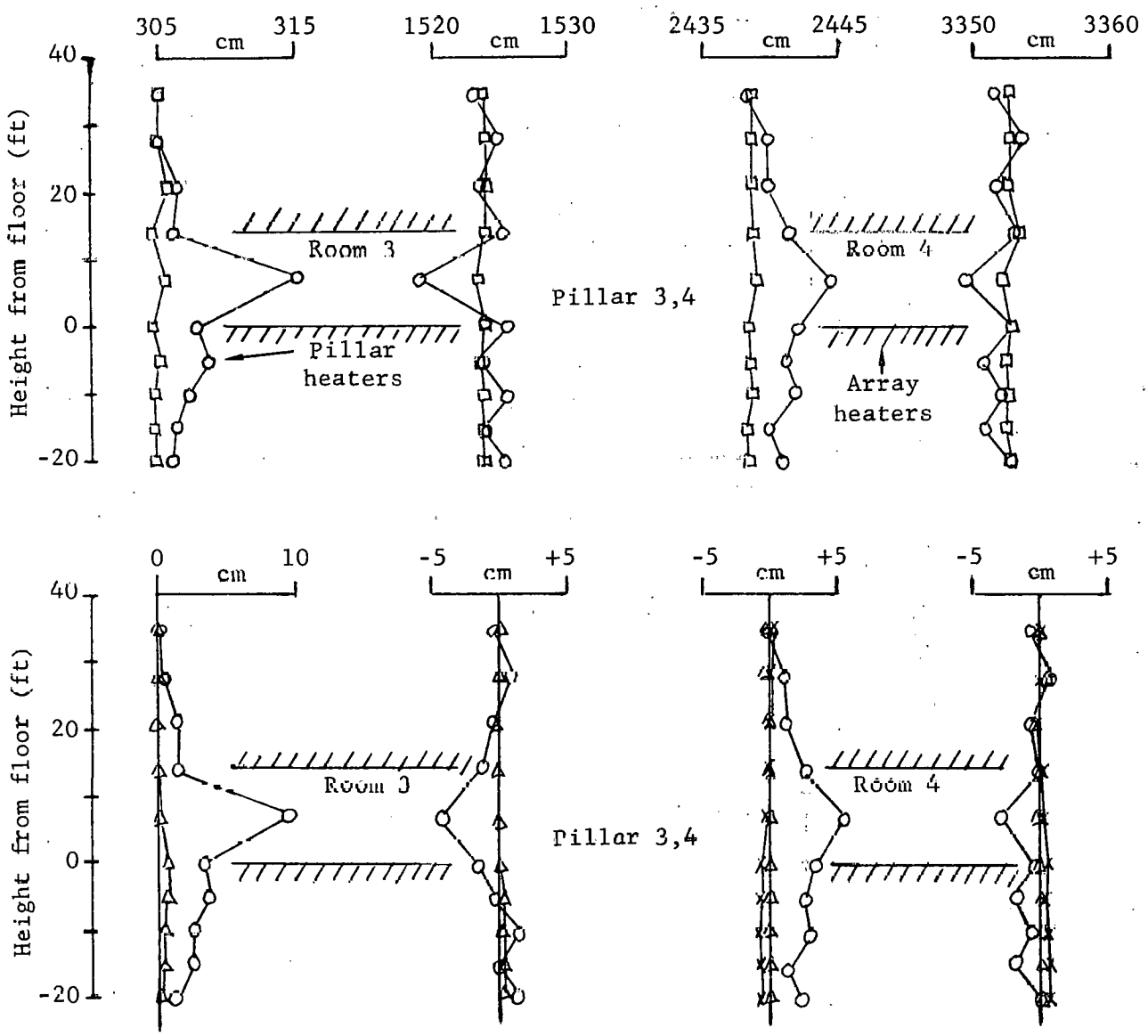

Figure 12. Horizontal deformation profiles along pillar wall sections.
(top) Profiles at day 806 and day 1500 with creep.
(bottom) Displacements with respect to day 806 for day 1354 and day 1500 without creep, and day 1500 with creep.

Schematics of Heated Pillar

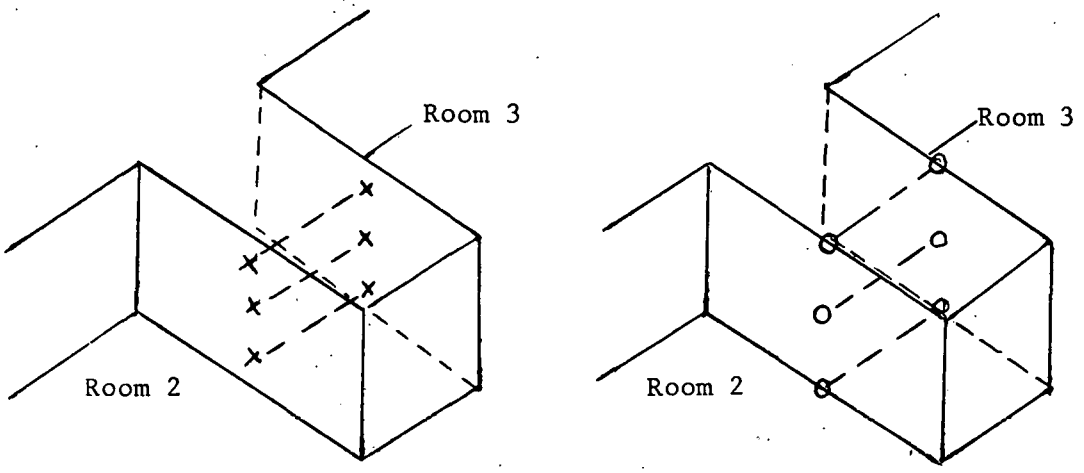

Heated pillar gage locations

Heated pillar grid points in first two simulations

Vertical Profiles of Horizontal Deformations in Heated Pillar

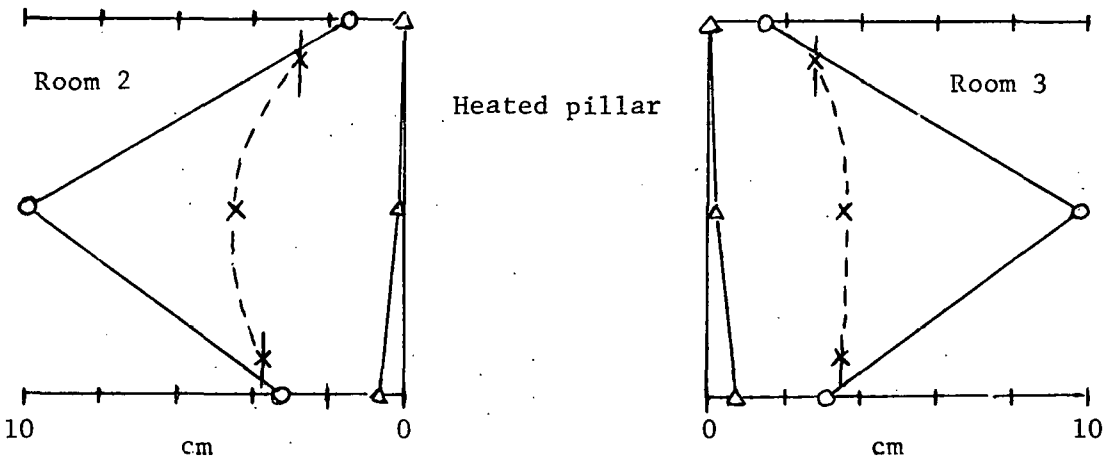

Horizontal deformation

Horizontal deformation

× Experimental data, Ref. 1, Figure 11.83

O Computed with creep

△ Computed without creep

Figure 13. Computed and experimental horizontal deformation of heated pillar walls from standard day 806 to 1500.

Figure 14 provides corresponding displays for the pillar thickening in rooms 1 and 4. Again, the discrepancies are not serious in view of earlier comments. Future simulations should contain a minimum of five points to define the pillar height if reasonable pillar thickness contours are required.

The vertical distortions around room 3 are displayed in Figure 15 for the case of creep. A different reference point was employed for this room and it was based on the following arguments.

The roof and floor profiles labeled A, B, and C in Figure 15 occurred before the pillar heaters were turned on at day 1170. Therefore, the response of room 3 up to this time was dominated by the large creep rate following the simulated excavation at day 806. To first order, the driving stress field around room 3 at early times was symmetrical about a horizontal plane through the pillar half-height. Thus, the roof sag and floor lift should have approximately a mirror symmetry until the pillar heaters are activated or until the array room heat effects reach room 3. It can be confirmed that the assumed stationary point of Figure 15 provides almost perfect mirror symmetry for contours A, B, and C in room 3 and in the heated pillar.

At later times, the rate of roof sag continues to diminish as the creep rate decreases. In contrast, the floor continues its vigorous rise (floor profiles D, E, and F) due to the activation of the pillar heaters on day 1170.

3.2 THERMAL RESPONSE

Computed temperature contours around the pillar heaters and the array heaters are compared with the corresponding PSV experimental contours in Figure 16. There is good quantitative agreement and an excellent qualitative agreement. The quantitative differences may be attributed to (1) the three-dimensionality of the experiment, (2) idealized convection model, and (3) the fact that the computed contours around the array heaters are shown for day 1353 instead of day 1382 when the array heaters were turned off.

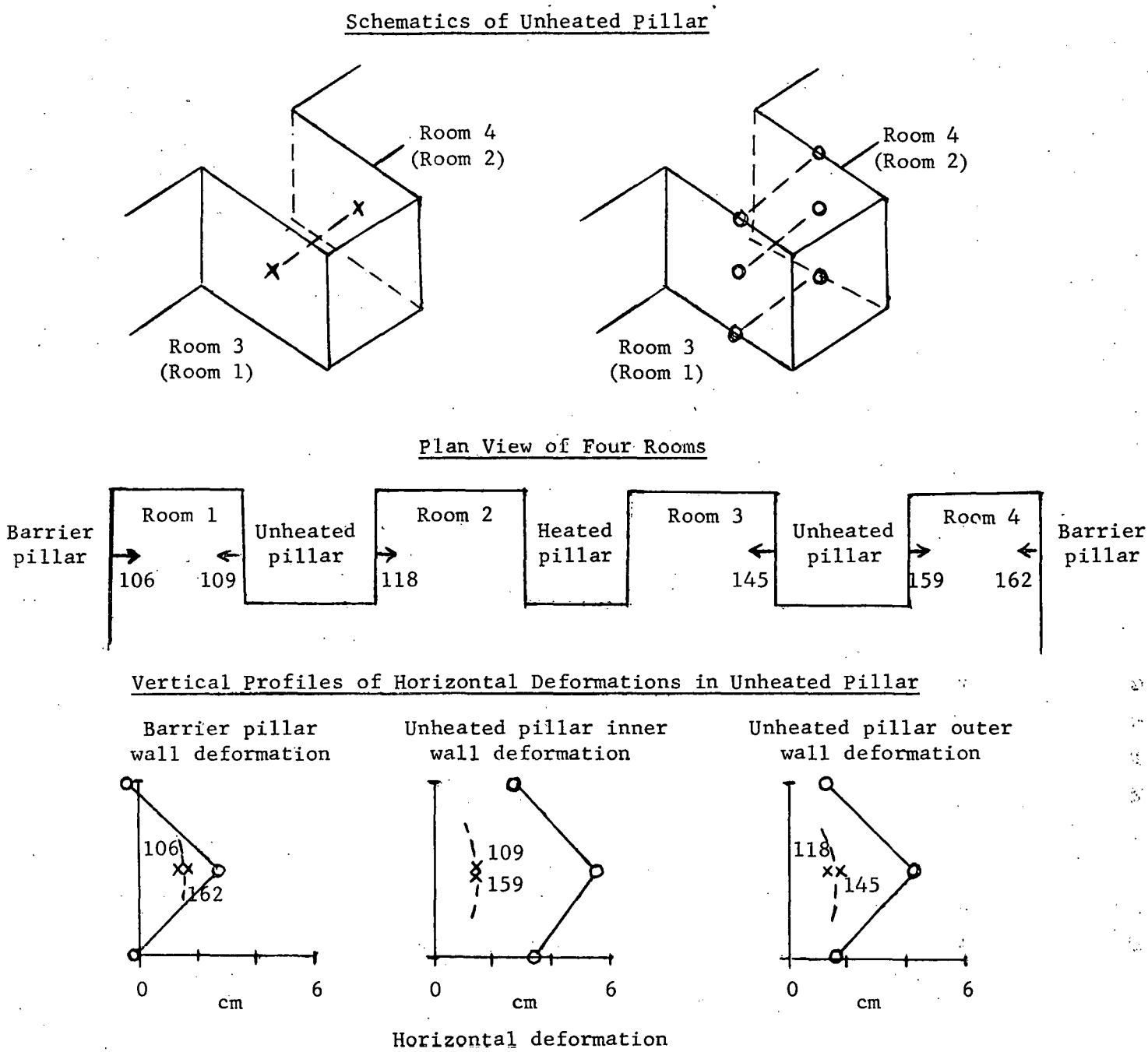

Figure 14. Computed and experimental horizontal displacements of pillar walls from standard day 806 to 1500.

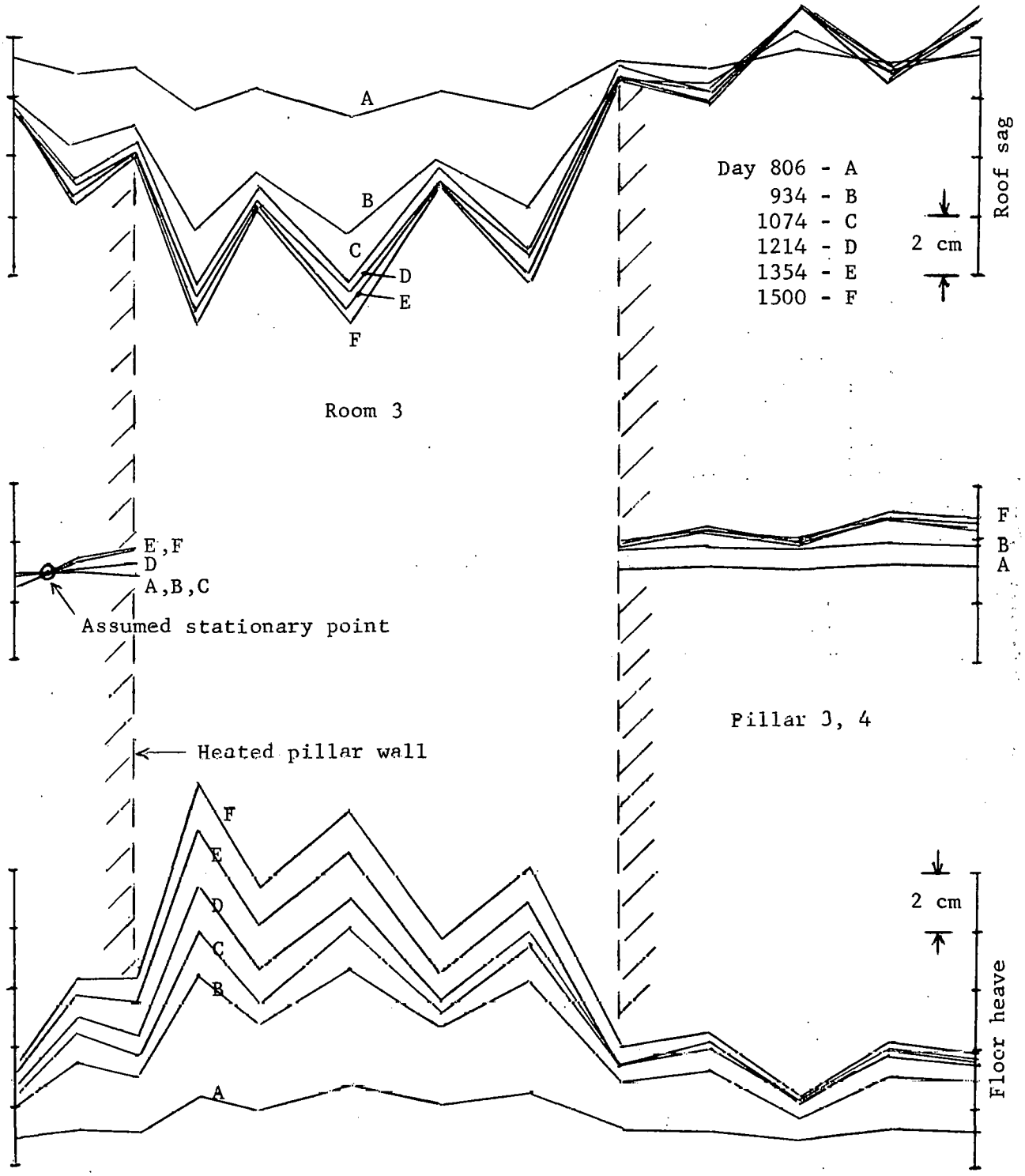

Figure 15. Vertical distortions in the vicinity of room 3 computed with creep and referenced to assumed stationary point in the heated pillar.

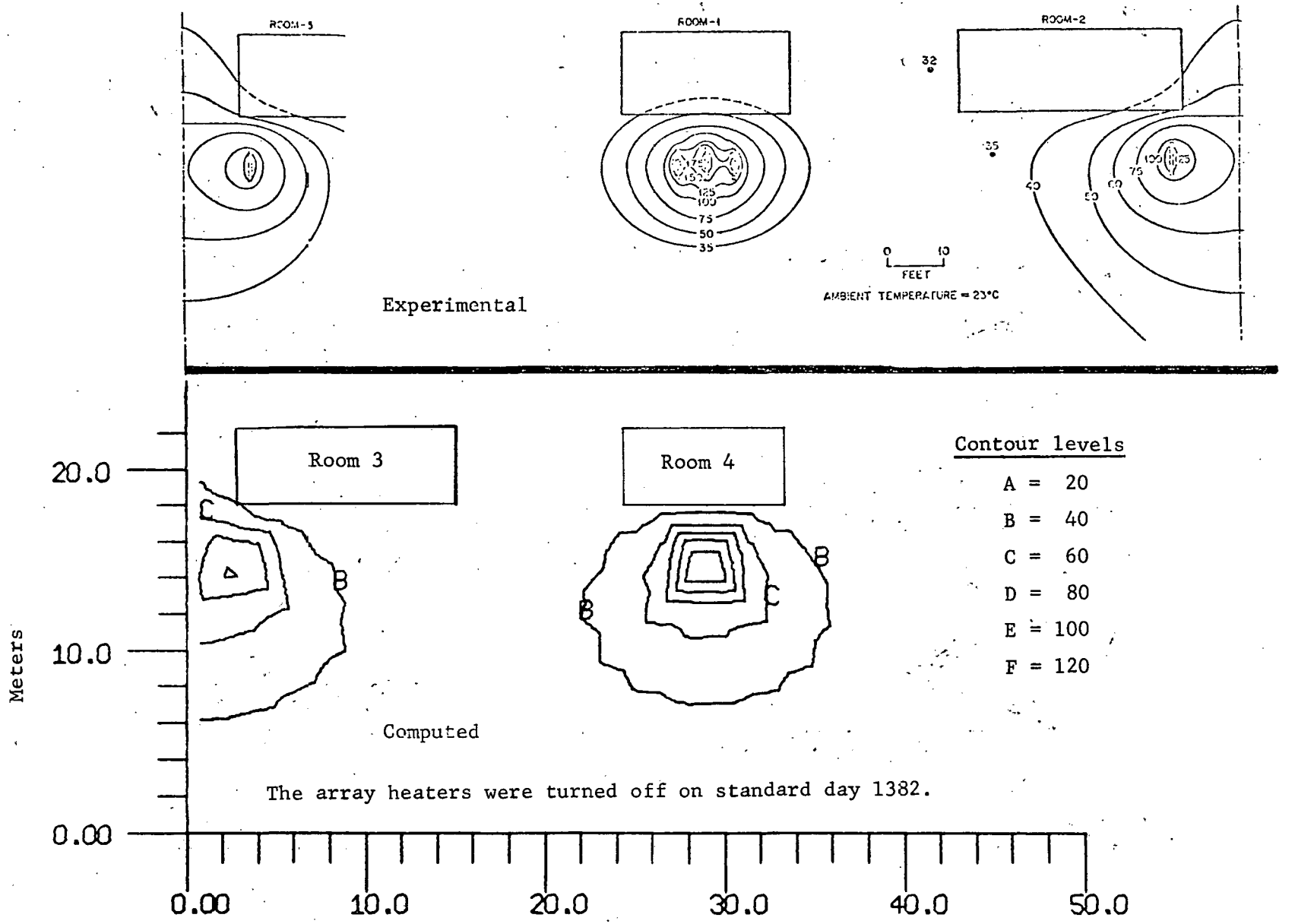

Figure 16. Computed temperature contours around array heaters (day 1353), pillar heaters (day 1500).

Temperature time histories at specific locations (i.e., gage locations) are compared in Figures 17 and 18. Once again, good agreement is seen between the experimental data and the computed results.

The convection losses to the rooms amounted to 51% of the total heat input (by the heaters) in a period of 23 months. The losses through the isothermal boundaries were 34% of the total heat. Therefore, the amount of heat remaining in the grid at the end of 23 months was about 15% of the total heat supplied to the grid. Note that the actual heat conducted at these artificial boundary locations would be a fraction of the 34% quoted above if the boundaries were placed farther out.

3.3 SENSITIVITY ANALYSIS

The sensitivity of the results to selected variations in input was established by repeating the creep calculation in a new grid, shown in Figure 1c. The selected input features are

- Two zones were added to the top of the grid to raise the top horizontal boundary by 14 ft (4.267 m) and two zones were added to the bottom to lower the bottom horizontal boundary by 16.32 ft (4.974 m). The boundaries were moved farther out in order to assess the influence of boundary nearness on the closure of the rooms.

- The two zones modeling the pillar height were replaced by three zones to provide more accuracy for room convergence.

- The bottom stress boundary condition was replaced by a horizontal roller (vertical velocity = 0) boundary in order to eliminate the float effect seen in the previous runs.

In addition, two minor errors were discovered in the original calculation and were corrected in the sensitivity analysis. The first error was that

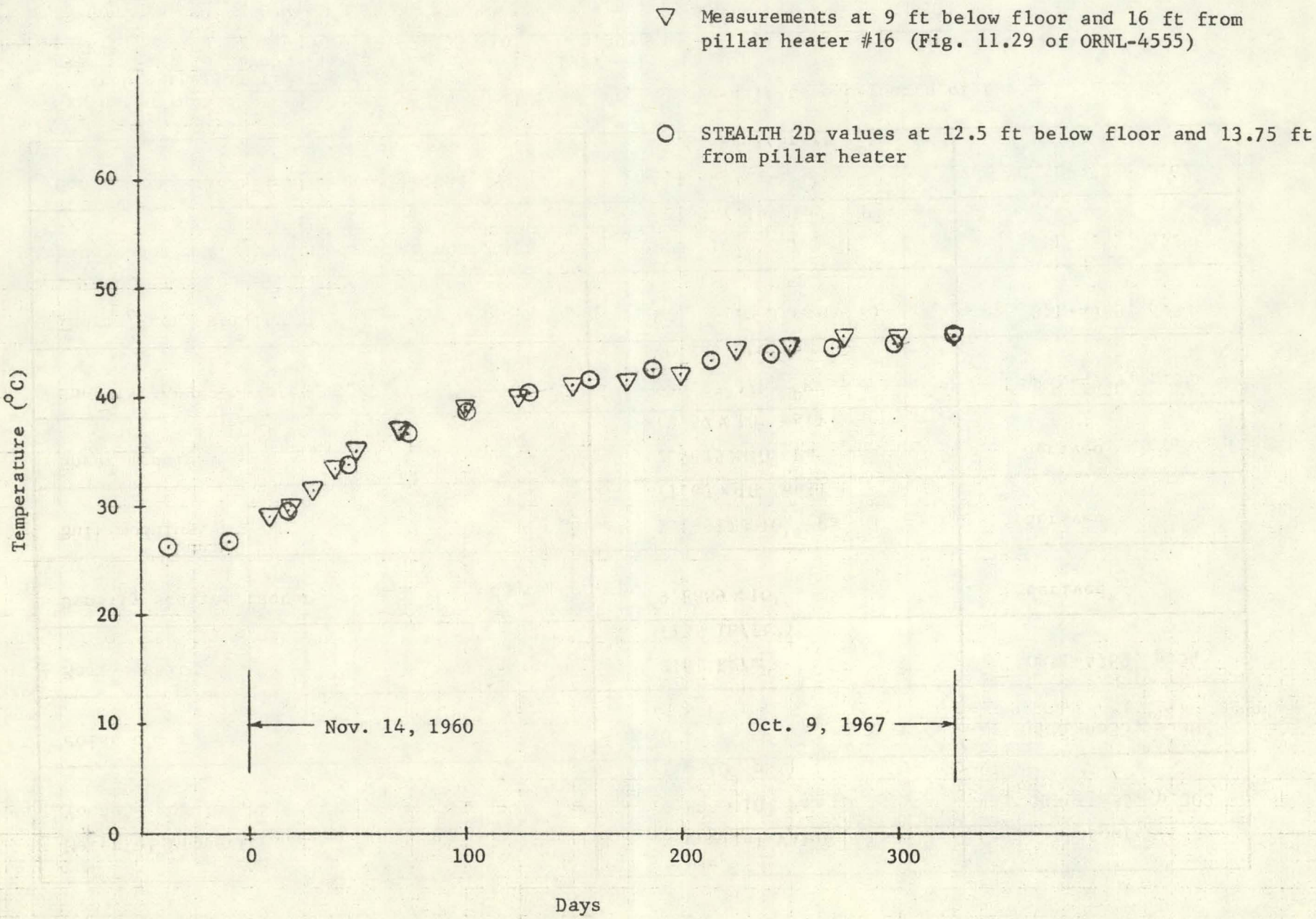

Figure 17. Temperature history comparison near pillar heater #16.

K+E 10 X 10 TO THE CENTIMETER
KEUFFEL & ESSER CO.
461510

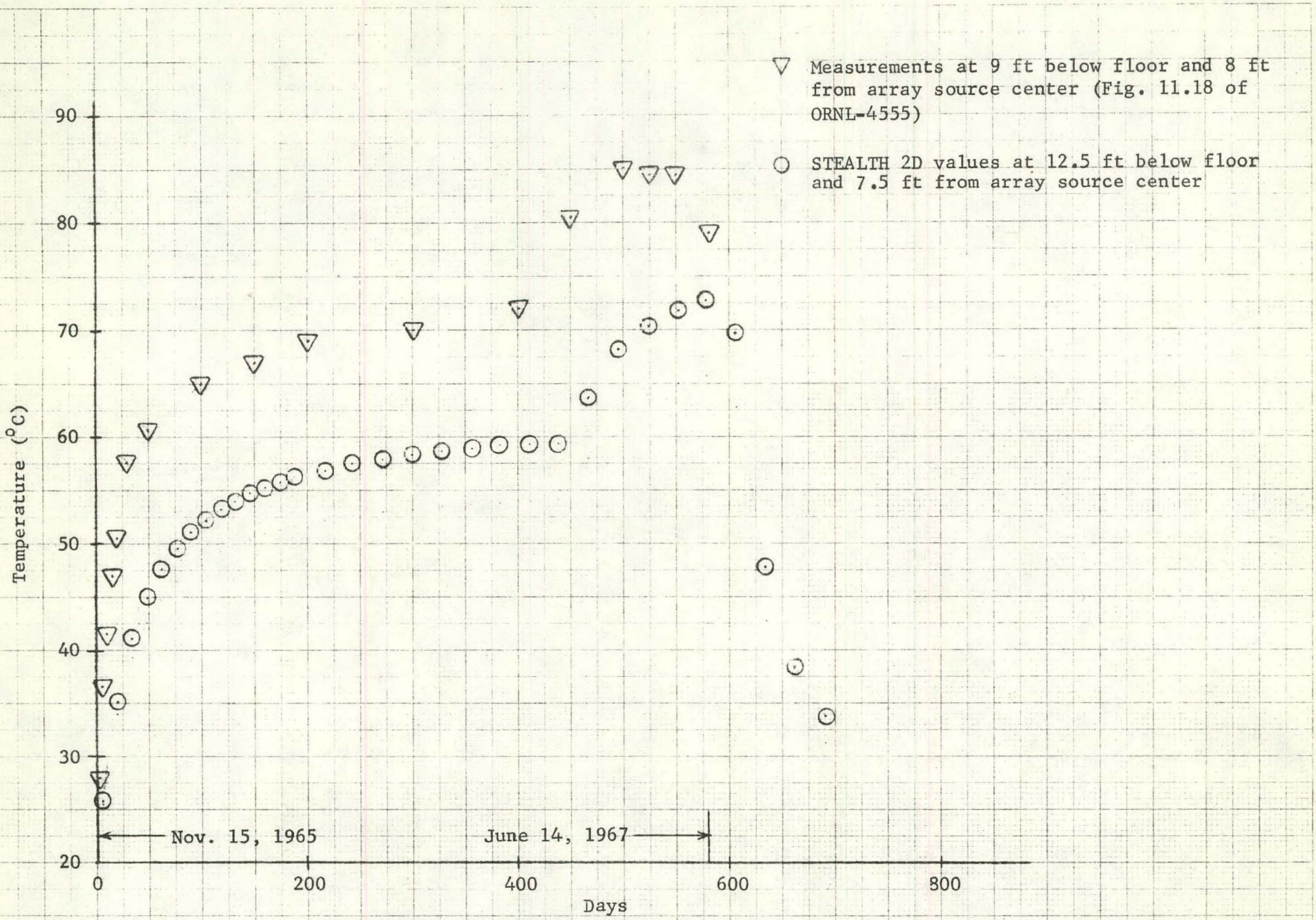

Figure 18. Temperature history comparison near array heaters.

the difference between the applied stresses on the upper and lower boundaries was based on one psi per foot of grid height, rather than on the product of mean density, height, and gravity. This error contributed to the annoying float effect, but did not affect the stresses in the vicinity of the rooms. The second error consisted of a misplaced bracket around the gravity term in the acceleration equation. This also enhanced the float effect but, again, was harmless with respect to room convergence.

The results of the sensitivity calculation showed that the more distant boundaries had very little effect on the rooms. The effect on temperature in the zones surrounding the rooms can be observed in Figures 19 and 20. The zoning of the original and sensitivity grids is identical in these figures except in the pillars. Taking this into account, it can be seen that the differences are a fraction of a degree. The temperatures above the rooms remain close to ambient (23°C) because of the mitigating effect of the room ventilation. The room ventilation effect is not as effective below the rooms and the temperature difference approaches several degrees at greater depths. This is due to the different locations of the bottom isothermal boundaries.

The differences in the stresses around the rooms can be substantial at any fixed time due to different phasing of the mechanical oscillations of the two grids. However, the average values were comparable. This is seen in Figures 21 and 22. These figures display the equivalent* stress $/\sqrt{3}$ versus time in the original and sensitivity grids in the middle of the floor of room 3 at a depth of 2.5 ft (0.76 m). It can be seen that the details are different but that the average values are similar. It should be recalled that dynamic relaxation was employed only in the initialization calculations to establish equilibrium during instantaneous excavation at day 806. The inclusion of dynamic relaxation after day 806 would probably be advantageous with respect to damping the oscillations shown in Figures 21 and 22.

The remaining figures display either spatial profiles at indicated times, or displacements referenced to the day 806 position. Figure 23 compares horizontal profiles at day 1500 in the original and sensitivity grids.

---

*See Appendix A for equivalent stress.

23.8	23.8	23.6	23.5	23.3	23.2	23.2	23.2	23.4	23.4
24.5	24.2	24.0	23.6	23.3	23.2	23.2	23.4	23.5	23.7
25.8	25.1	23.9	23.3	23.1	23.1	23.1	23.2	23.8	24.0
29.6	26.8	Room 3 Original Grid						23.8	24.9
42.1	32.6							24.5	26.4
62.0	57.2	41.9	37.3	29.9	26.7	25.4	25.0	27.2	27.8
74.5	94.3	87.0	53.2	38.4	31.9	28.2	28.3	28.0	29.8
79.4	102.	95.8	60.1	45.1	34.5	31.8	29.2	30.4	30.4

23.9	23.9	23.7	23.6	23.4	23.3	23.3	23.3	23.5	23.5
24.5	24.2	24.0	23.6	23.3	23.2	23.2	23.4	23.5	23.7
25.8	25.1	23.8	23.3	23.1	23.1	23.1	23.2	23.8	24.1
29.0	26.1	Room 3 Sensitivity Grid						23.7	24.9
34.2	28.7							24.1	25.7
44.8	35.3							24.9	26.9
61.3	55.2	42.1	37.3	30.0	26.8	25.6	25.2	27.2	28.1
73.9	94.2	86.6	53.6	38.6	32.2	28.6	28.7	28.4	30.2
79.5	102.	96.3	60.3	45.6	35.0	32.4	29.8	31.1	31.0

Figure 19. Temperatures at day 1500 in the zones surrounding room 3 in the original grid (top) and the sensitivity grid (bottom).

23.4	23.4	23.3	23.3	23.3	23.3	23.4	23.5	23.7	23.9
23.7	23.5	23.4	23.3	23.2	23.3	23.4	23.6	23.9	24.3
24.1	23.7	23.3	23.1	23.1	23.1	23.2	23.4	24.1	24.8
24.9	23.9	Room 4 Original Grid						24.1	25.5
26.7	24.8							24.8	27.7
28.5	28.2	26.2	25.9	25.9	25.8	26.0	26.3	28.5	29.0
30.2	30.7	30.5	30.3	30.2	30.3	30.3	30.7	30.7	31.1
32.3	32.7	33.7	33.6	34.0	33.8	33.8	33.5	33.2	32.6

23.5	23.5	23.4	23.4	23.4	23.4	23.6	23.7	23.9	24.2
23.7	23.6	23.5	23.3	23.3	23.4	23.5	23.8	24.0	24.6
24.1	23.8	23.3	23.2	23.1	23.1	23.2	23.5	24.2	25.0
24.9	23.8	Room 4 Sensitivity Grid						24.0	25.7
25.8	24.2							24.4	26.5
27.2	25.4							25.3	28.0
28.9	28.2	26.4	26.0	26.0	26.0	26.1	26.5	28.4	29.5
30.6	31.2	30.8	30.8	30.6	30.7	30.8	31.1	31.3	31.5
33.0	33.4	34.5	34.3	34.7	34.6	34.5	34.4	33.9	33.5

Figure 20. Temperatures at day 1500 in the zones surrounding room 4 in the original grid (top) and the sensitivity grid (bottom).

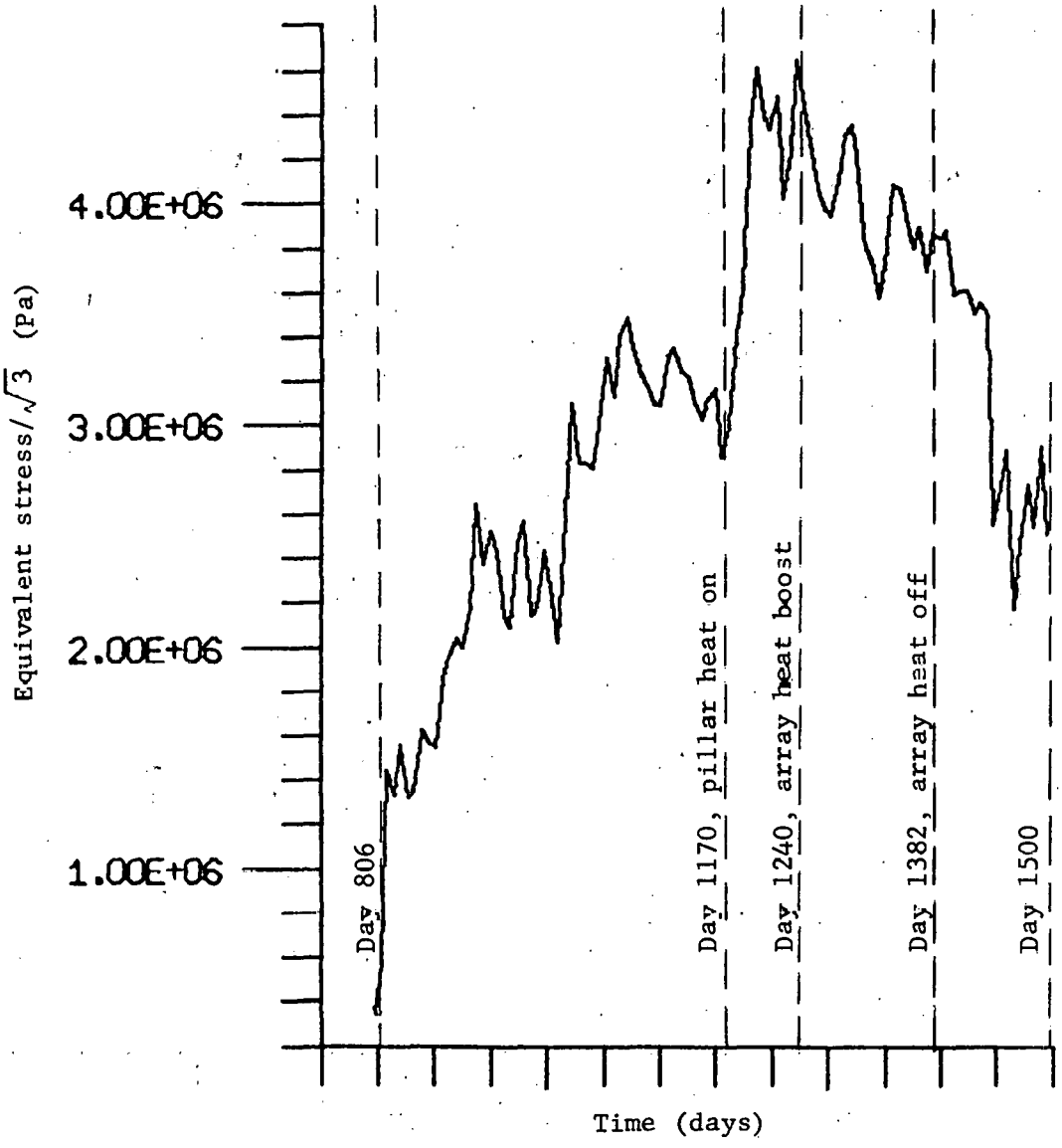

Figure 21. Equivalent stress/$\sqrt{3}$ (Pascals) versus time (days) in the original grid in the middle of room 3 at a depth of 2.5 feet below the floor.

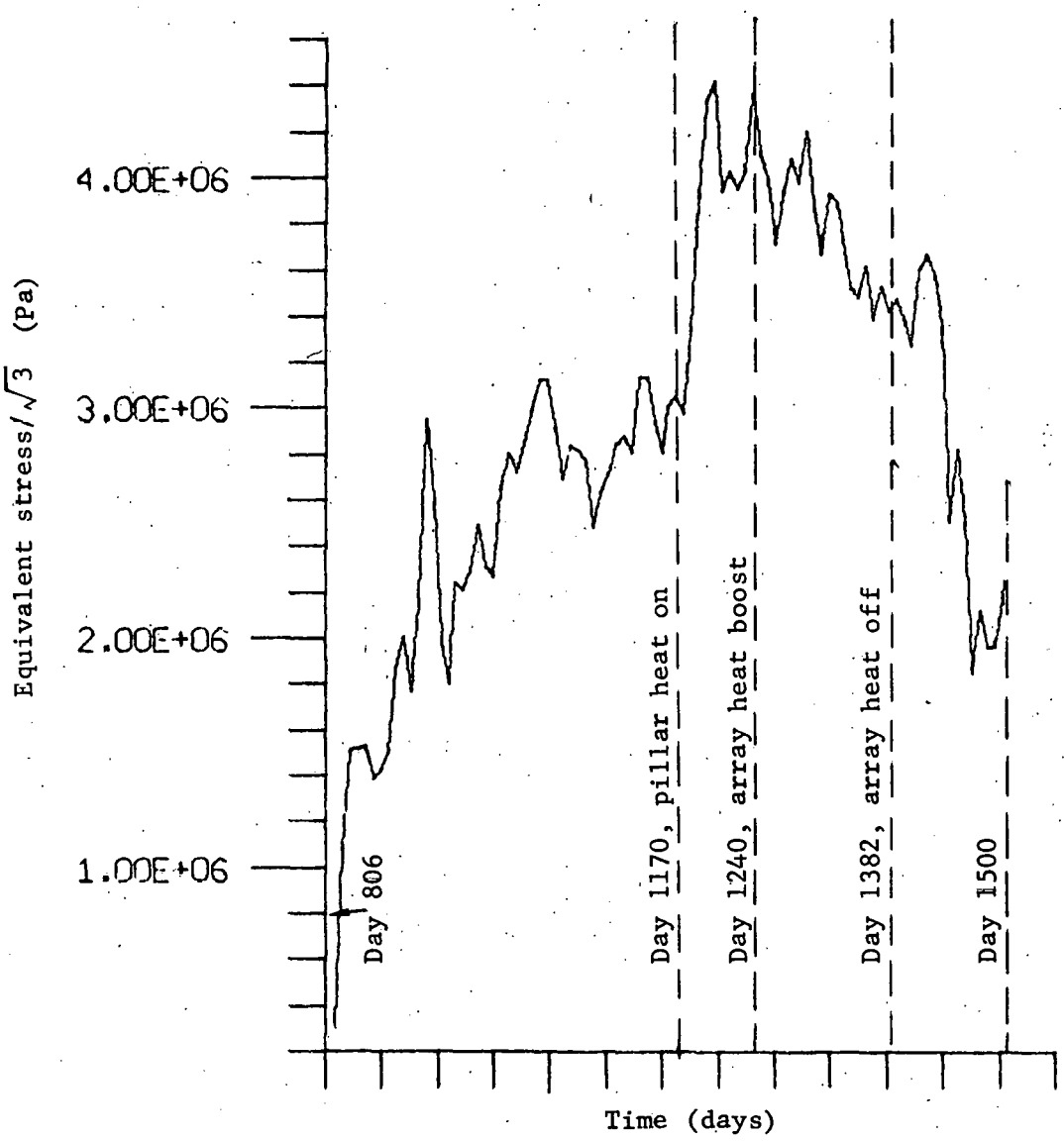

Figure 22. Equivalent stress/$\sqrt{3}$ (Pascals) versus time (days) in the sensitivity grid in the middle of room 3 at a depth of 2.5 feet below the floor.

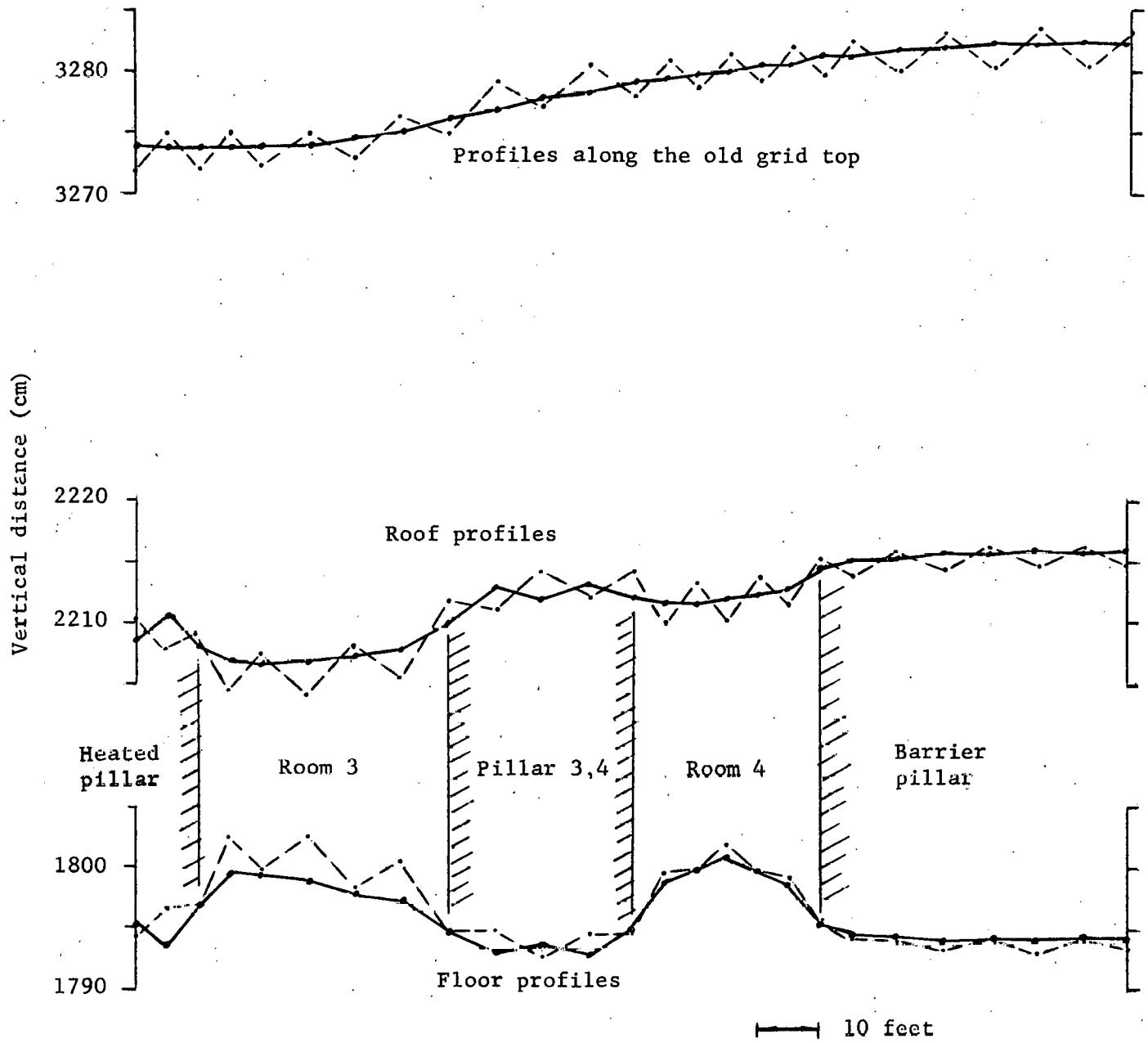

Figure 23. Comparisons of horizontal profiles at day 1500 for the original grid (dashed) and the sensitivity grid (solid).

The zigzag effect in the old grid is markedly reduced in the sensitivity grid. This is due to the fact that the sensitivity grid employed a bottom roller boundary condition in place of the bottom grid stress boundary condition. This new boundary condition also prevented the new grid from floating and no benchmark assumptions had to be employed to obtain relative displacements. Figure 23 is a summary comparison of the creep data in Figure 5.

Figure 24 compares vertical profiles at day 1500 in the two grids. Again, it can be seen that the new grid is much smoother with respect to the zigzag effect. Figure 24 is a summary comparison of the creep data in Figure 12.

Figure 25 compares roof and floor contours around room 3 at day 806 and day 1500 for the two grids. Ignoring the zigzag difference, it can be seen that the new grid has slightly less room convergence. This is probably due to the finer zoning in the pillars and not to the small stress and temperature differences.

Figure 26 compares the array room floor uplift and roof sag for the two grids. It is not clear whether or not there is a significant difference in the room convergence.

Figure 27 compares the pillar wall horizontal displacements for the two grids. Now the zoning effect is obvious. The original grid tended to buckle with its single intermediate point achieving a large displacement. The sensitivity grid with its two points responded more smoothly and with less displacement, in better agreement with the experimental data.

The overall assessment of the sensitivity results indicates that

1. The original and sensitivity boundaries were both sufficiently distant with respect to stress and temperature at the room locations.

2. The bottom roller boundary condition is superior to the previous stress condition because it eliminates the zigzag effect as well as the float.

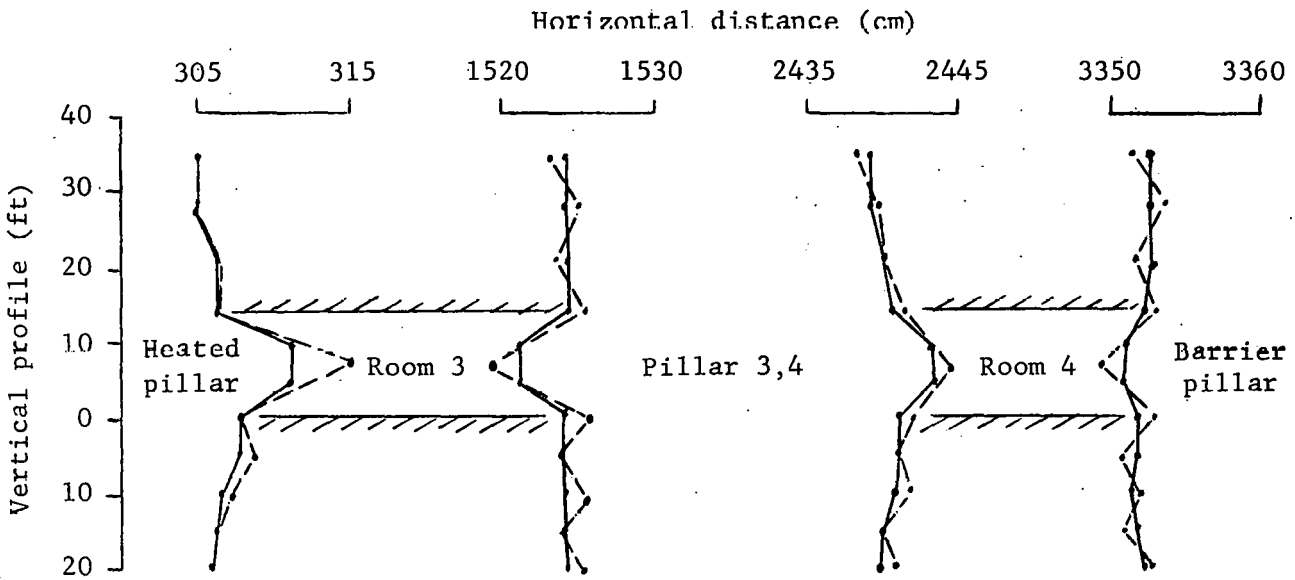

Figure 24. Comparisons of vertical profiles through the pillar walls at day 1500 for the original grid (dashed) and the sensitivity grid (solid).

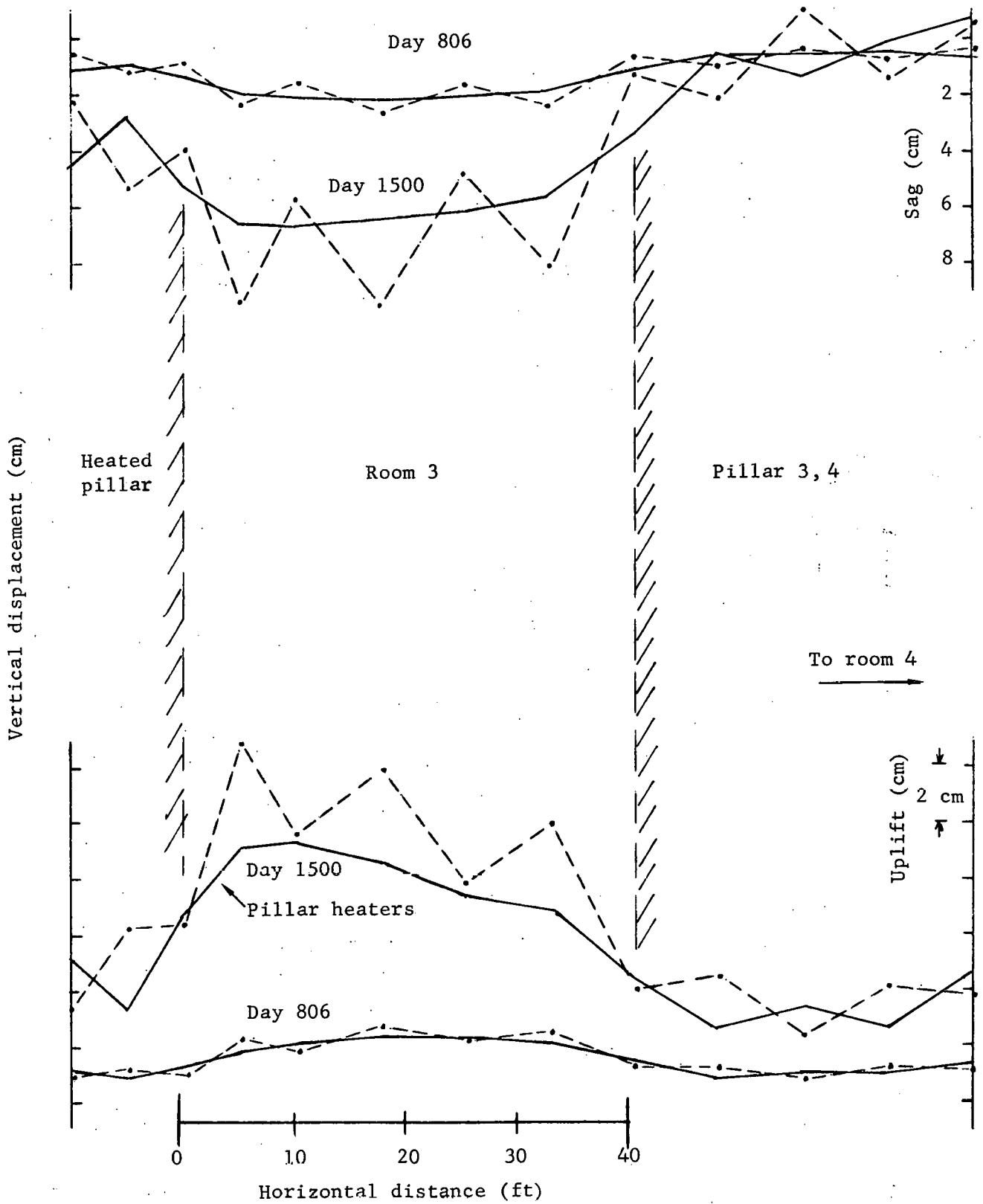

Figure 25. Room 3 roof and floor contours for original grid (dashed) and sensitivity grid (solid) at day 806 and day 1500.

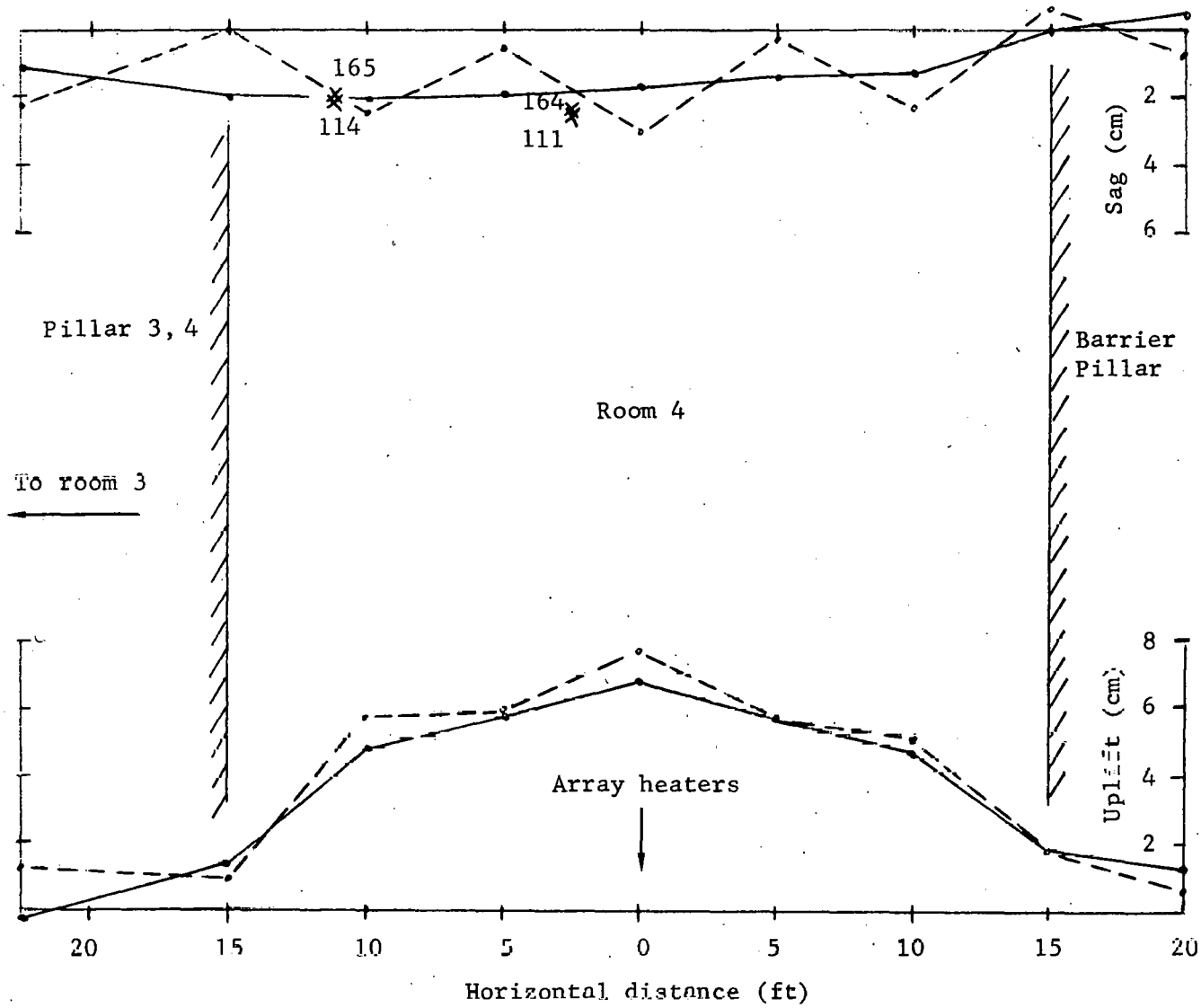

Figure 26. Comparisons of array room floor uplift and roof sag from day 806 to day 1500 for original grid (dashed), sensitivity grid (solid), and gages (crosses).

Vertical Profiles of Horizontal Deformation in Heated Pillar

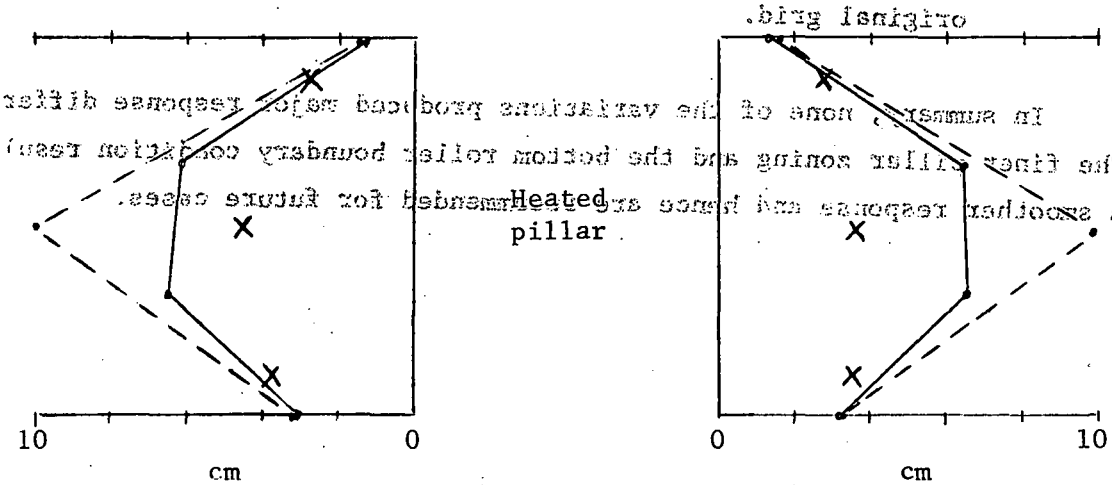

(a) Heated pillar wall. See Figure 13 for gage locations.

Vertical Profiles of Horizontal Deformation in Unheated Pillar

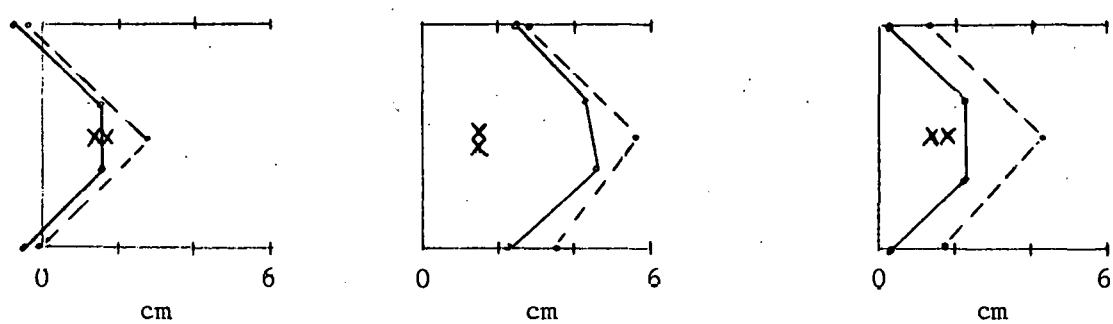

(b) Cold pillar walls. See Figure 14 for gage locations.

Figure 27. Comparison of pillar wall horizontal displacements from day 806 to day 1500 for original grid (dashed), sensitivity grid (solid), and experiment (crosses).

3. The finer zoning in the pillars resulted in less horizontal displacement which probably accounts for the slightly smaller convergence in room 3 in the sensitivity grid compared to original grid.

In summary, none of the variations produced major response differences. The finer pillar zoning and the bottom roller boundary condition resulted in a smoother response and hence are recommended for future cases.

SECTION 4
CONCLUSIONS

The simulation of the Project Salt Vault experiment as described in this report demonstrates the applicability of the explicit finite-difference technique to be of predictive value for simulating the thermomechanical response of nuclear waste repositories. Both thermal-elastic and thermal-elastic-creep models were successfully employed and the simulation data were compared to measured values derived from the Project Salt Vault experiment. Agreement with PSV floor heave and roof fall measurements was exceptionally good in both shape and magnitude, considering the non-essential limitations that were employed for expediency. It is believed that these results are unique in that no other contractor has ever predicted these measurements with such a complete set of realistic models.

The explicit calculational technique which was demonstrated was used in a strictly "predictive" mode. That is, all material property data, boundary conditions, zoning, etc., for the simulation were determined a priori. Then, a predictive simulation was performed in which no parameters were tuned, in order to achieve the agreement shown in this report. This, it is believed, clearly demonstrates the power of the explicit finite-difference method.

Since this was a demonstration calculation, only certain sensitivities were explored. Therefore, it is recommended that the following items be explored before full three-dimensional modeling is undertaken:

1. The time-dependent excavation sequence should be modeled. In this simulation, all four rooms should be included.

2. The creep model should be calibrated to additional experimental data, if available.

3. For demonstration purposes, the zoning was chosen to be particularly coarse. In future simulations, at least the sensitivity to more finely zoned pillars should be investigated.

4. No attempt was made to optimize the computing efficiency. For example, it is possible to increase the efficiency of the solution of the creep equations. In addition, an alternate method of density scaling that essentially allows one to use a variable (rather than a fixed) density scaling factor should enhance the equilibration of stresses.

REFERENCES

1. R. L. Bradshaw and W. C. McClain, eds., "Project Salt Vault: A Demonstration of the Disposal of High-Activity Solidified Wastes in Underground Salt Mines," ORNL-4555, Oak Ridge National Laboratory, Oak Ridge, Tennessee, April 1971.

2. A. M. Starfield and W. C. McClain, "Project Salt Vault: A Case Study in Rock Mechanics," Int. J. Rock Mech. Min. Sci. and Geomech. Abstr., 10, 1973 (641-657).

3. Ronald Hofmann, "STEALTH, A Lagrange Explicit Finite-Difference Code for Solids, Structural, and Thermohydraulic Analysis," Vols. 1, 2, and 3, EPRI NP-260, Electric Power Research Institute, Palo Alto, California, August 1976.

4. Mark L. Wilkins, "The Use of Artificial Viscosity in Multidimensional Fluid Dynamic Calculations," Preprint UCRL-78348, Lawrence Livermore Laboratory, Livermore, California, October 21, 1976. Paper prepared for submission to J. Comp. Phys.

APPENDIX A
CREEP MODELING

A.1 INTRODUCTION

A creep model has been developed which, when given constitutive constants for salt derived from laboratory salt pillar experiments and used in conjunction with an EFD code, gives excellent agreement with data from a field test called Project Salt Vault (PSV). The PSV numerical simulations using the creep model applied to salt are reported in the main body of this report. This appendix contains a discussion of the physical and theoretical basis for the model as well as a description of the numerical procedure used to integrate the creep formulas.

A.2 PHYSICAL AND THEORETICAL BASIS FOR THE MODEL

The laboratory pillar experiments of Lomenick, reported in Reference 1, provided the basis for both the SAI model and the Starfield-McClain (S&M) model of Reference 2. The experimental configurations were small-scale mock-ups of cylindrical salt pillars, as shown schematically in the diagrams of Figure A-1. The time-dependent strain of the pillar height, defined by the gap distance, x, was obtained for different conditions of temperature and average vertical stress in the pillar. The temperatures ranged from about 20 to 200 degrees Centigrade. The vertical stress ranged from zero to about 4.14×10^7 Pa (6000 psi) and was defined by the ratio of the load to the cross-sectional area of the pillar.

The vertical stress was applied suddenly in all of these experiments and was not varied during a given experiment. It would have been desirable if the stress had been changed while creep was occurring in some of the experiments. This was not done, and assumptions had to be employed to model this feature. The S&M and SAI models employed different assumptions and,

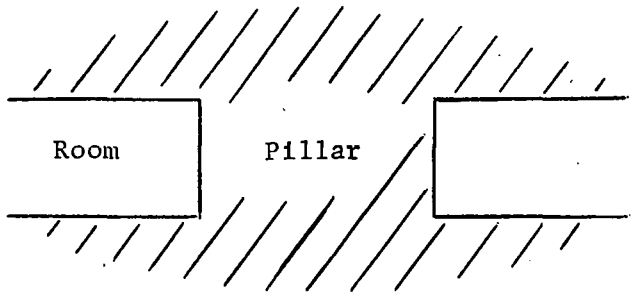

(a) In-situ cylindrical salt pillar.

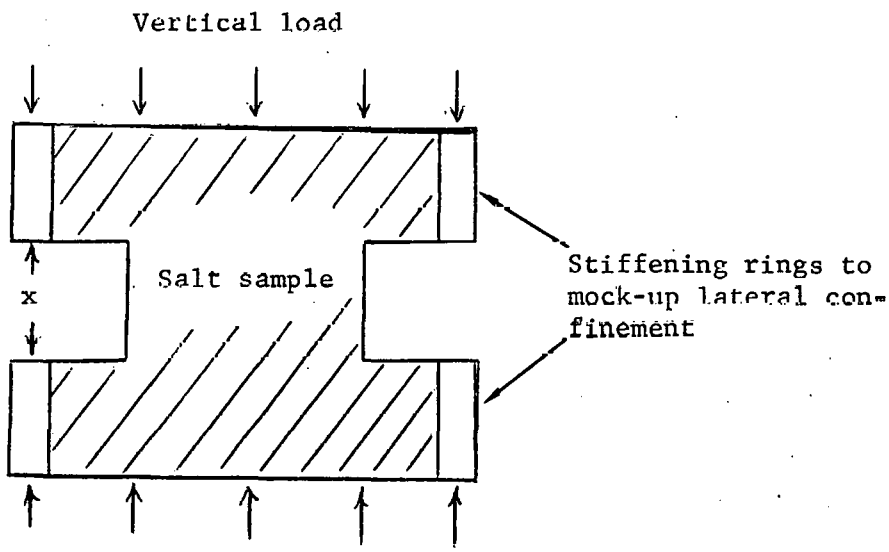

(b) Small-scale mock-up of pillar region.

Figure A-1. Schematic geometry of small-scale experiments.

consequently, predict different creep responses for stress changes, as will be seen later. Fortunately, the temperature was changed while creep was occurring in some of these experiments. Consequently, the S&M and SAI models are identical with respect to this feature.

The diagrams of Figure A-2 illustrate a case of constant temperature. Figure A-2(a) shows the applied conditions. The pillar creep strain, ϵ_x, and creep strain rate, $\dot{\epsilon}_x$, are shown schematically in Figures A-2(b) and A-2(c), and can be fit by the forms

$$\epsilon_x = A(t - t_o)^a \ \theta^b \sigma_x^c \tag{A-1a}$$

$$\dot{\epsilon}_x = a\, \epsilon_x / (t - t_o) \tag{A-1b}$$

where a, b, and c are material constants, while the value of A depends on the geometry as well as on the material; t is time; θ is temperature; and σ_x is the vertical pillar load in stress units.

The diagrams of Figure A-3 display a case with a temperature jump at t_1. The observed response can be fit as an overlay of two constant temperature cases with a time shift to provide creep strain continuity at t_1. The creep strain and its rate after t_1 can be fit by the forms

$$\epsilon_x(t > t_1) = A(t - \lambda)^a \theta_1^b \sigma_o^c \tag{A-2a}$$

$$\dot{\epsilon}_x(t > t_1) = a\, \epsilon_x / (t - \lambda) \tag{A-2b}$$

where the value of λ provides creep strain continuity at t_1. Hence, λ can be obtained from Eqs. (A-1a) and (A-2a) as follows,

$$(t_1 - t_o)^a \theta_o^b \sigma_o^c = (t_1 - \lambda)^a \theta_1^b \sigma_o^c .$$

The previous expressions can then be generalized for continuous temperature

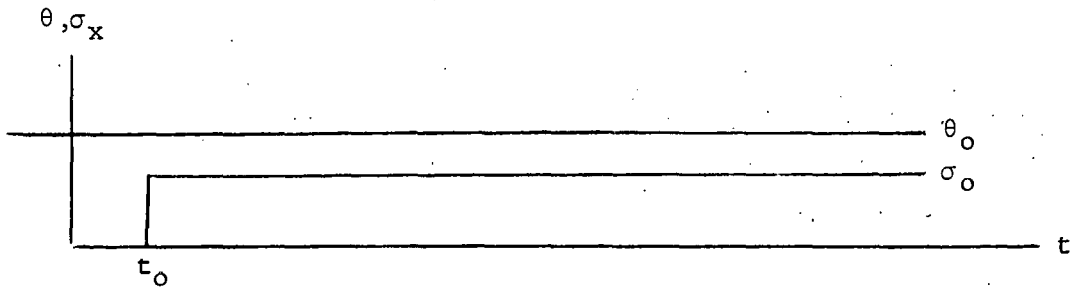

(a) Imposed conditions of temperature and stress.

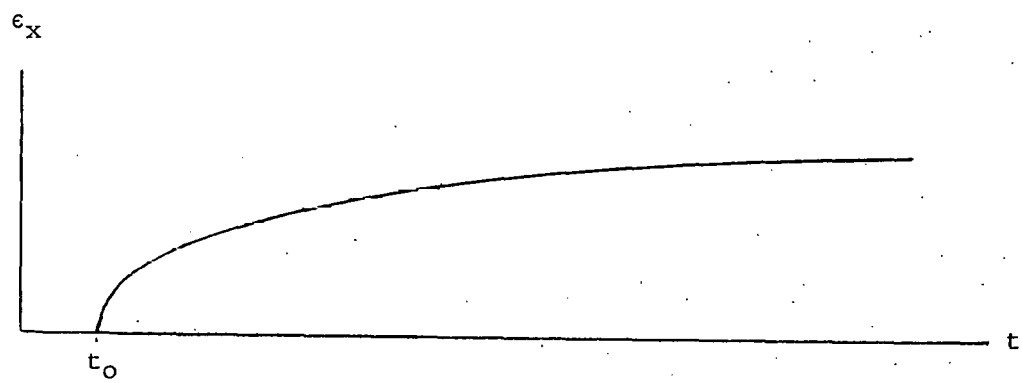

(b) Creep strain response.

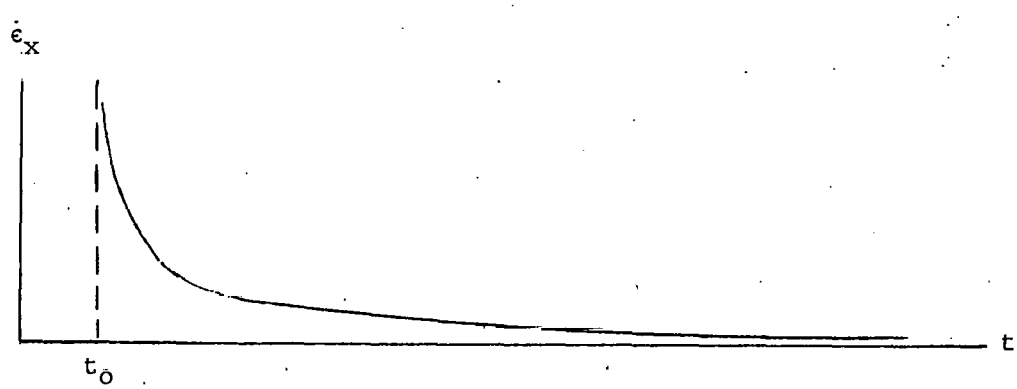

(c) Creep strain rate response.

Figure A-2. Schematics of constant temperature case.

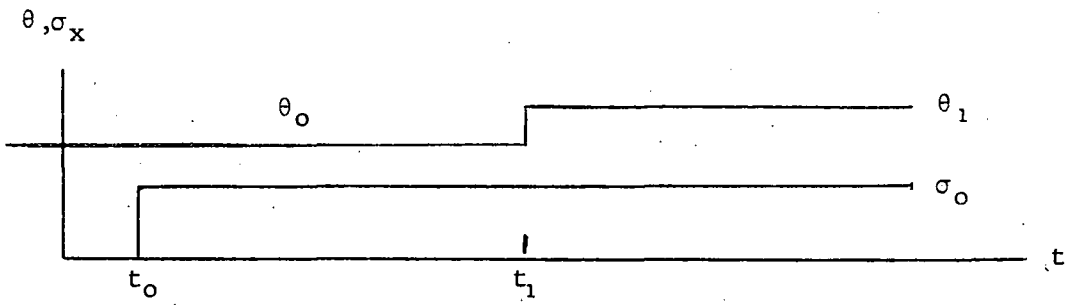

(a) Imposed conditions of temperature and stress.

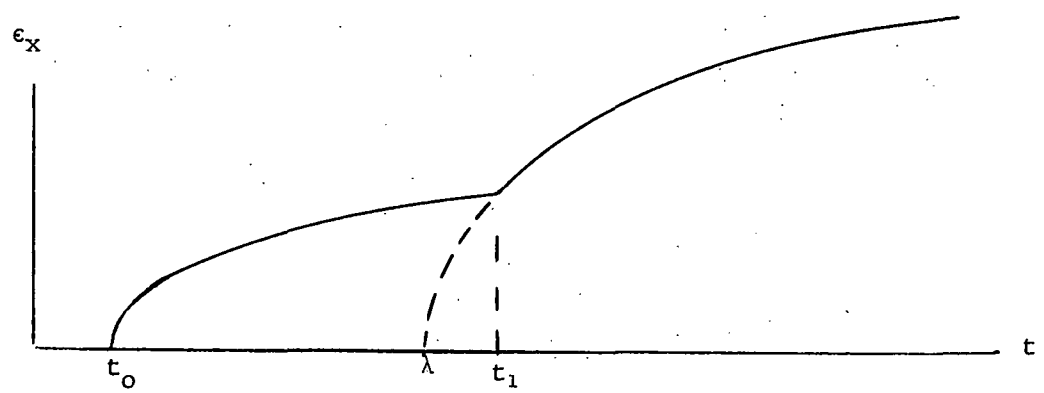

(b) Creep strain response.

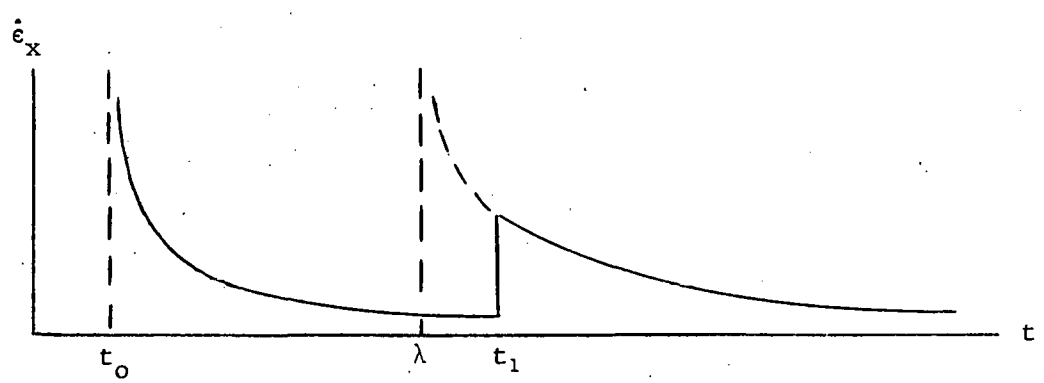

(c) Creep strain rate response.

Figure A-3. Schematics of temperature jump case.

changes (with constant stress) by the differential expressions

$$d\epsilon_x = \frac{\partial \epsilon_x}{\partial t} dt + \left[\frac{\partial \epsilon_x}{\partial \lambda} d\lambda + \frac{\partial \epsilon_x}{\partial \theta} d\theta \right]$$

$$= \frac{a\epsilon_x}{t-\lambda} dt + \left[- \frac{a\epsilon_x \, d\lambda}{t-\lambda} + \frac{b\epsilon_x \, d\theta}{\theta} \right] .$$

By definition, a finite change of creep strain requires a finite time interval and the sum of the terms in the bracket is identically zero. Thus, the SAI and S&M pillar models for constant stress with temperature changes can be expressed as

$$\epsilon_x(\text{const } \sigma_x) = A\left[t - \lambda(t)\right]^a \left[\theta(t)\right]^b \sigma_o^c \tag{A-3a}$$

$$\dot{\epsilon}_x = a\, \epsilon_x / \left[t - \lambda(t)\right] \tag{A-3b}$$

where

$$\lambda(\text{const } \sigma_x) = \lambda(t_o) + \int_{t_o}^{t} (t - \lambda) \frac{b}{a} \frac{\dot{\theta}}{\theta} dt .$$

The SAI and S&M models depart for the case of variable stress. In analogy to the variable temperature case, the SAI model assumes that the response for variable temperature as well as for variable stress can be expressed as

$$d\epsilon_x = \frac{\partial \epsilon_x}{\partial t} dt + \left[\frac{\partial \epsilon_x}{\partial \lambda} d\lambda + \frac{\partial \epsilon_x}{\partial \theta} d\theta + \frac{\partial \epsilon_x}{\partial \sigma_x} d\sigma_x \right]$$

$$= \frac{a\epsilon_x}{t-\lambda} dt + \left[\frac{-a\epsilon_x}{t-\lambda} d\lambda + b\epsilon_x \frac{d\theta}{\theta} + c\epsilon_x \frac{d\sigma_x}{\sigma_x} \right] .$$

The sum of the terms in the bracket must be zero by creep strain continuity. Then the SAI pillar creep model for variable temperature and stress becomes

$$\epsilon_x = A\left[t - \lambda(t)\right]^a \left[\theta(t)\right]^b \left[\sigma_x(t)\right]^c \tag{A-4a}$$

$$\dot{\epsilon}_x = a\,\epsilon_x/(t - \lambda) \tag{A-4b}$$

$$\lambda(t) = \lambda_o + \int_{t_o}^{t} \left(\frac{t - \lambda}{a}\right) \left[b\,\frac{\dot{\theta}}{\theta} + c\,\frac{\dot{\sigma}_x}{\sigma_x}\right] dt\,. \tag{A-4c}$$

The analogous treatment of θ and σ_x in the SAI model is not present in the S&M model. The S&M model assumes that a change of stress (at constant temperature) occurring at τ produces a change of creep strain at $t \geq \tau$, according to

$$d\epsilon_x(t \geq \tau) = A(t - \tau)^a\,\theta_o^b\,d\left[\sigma_x(\tau)\right]^c$$

or

$$\epsilon_x(t \geq \tau) = \epsilon_x(\tau) + d\epsilon_x(t \geq \tau)\,.$$

The generalization for variable stress and temperature results in the S&M pillar creep model,

$$\epsilon_x = A \int_{t_o}^{t} \left[\int_{\tau}^{t} \theta^{b/a}\,(u)\,du\right]^a \frac{\partial}{\partial\tau}\left[\sigma_x(\tau)\right]^c d\tau\,. \tag{A-5}$$

It can be shown that the SAI and S&M pillar creep models of Eqs.(A-4) and (A-5) are identical for constant stress cases.* In addition, they converge to the same result for variable stress cases as time unfolds beyond the last stress change. The S&M model predicts infinite creep rate at stress jumps applied during creep, in contrast to the SAI model. Both models predict finite creep rate at temperature jumps applied during creep. Stress jump experiments would be required to select the most accurate model.

A.3 NUMERICAL CONSIDERATIONS

The steps to implement the SAI model numerically are:

- Generalize the SAI pillar model for geometric invariance for application to arbitrary configurations.
- Include the relations for stress relaxation due to creep strain.
- Express the total model in appropriate difference form for inclusion in a time-explicit, finite-difference code.

In order to generalize the SAI pillar model [Eq.(A-4)], the pillar creep strain, ϵ_x, must be replaced by an equivalent deviatoric strain, $\sqrt{3} < e >$, so that

$$< e > \equiv \sqrt{\frac{1}{2}\left(e_{xx}^2 + e_{yy}^2 + e_{zz}^2\right) + e_{xy}^2 + e_{yz}^2 + e_{zx}^2}$$

where e_{ij} are the deviatoric strain components, and the pillar load, σ_x,

*when a constant value of σ_x is applied suddenly at t_o.

must be replaced by an equivalent deviatoric stress, $\sqrt{3} < s >$, so that

$$< s > \equiv \sqrt{\frac{1}{2}\left(s_{xx}^2 + s_{yy}^2 + s_{zz}^2\right) + s_{xy}^2 + s_{yz}^2 + s_{zx}^2}$$

where s_{ij} are the deviatoric stress components. Assuming that creep is purely deviatoric, the invariant form of the SAI pillar model becomes

$$< e^{cr} > = A\left[t - \lambda(t)\right]^a \left[\theta(t)\right]^b \left[< s(t) >\right]^c , \tag{A-6a}$$

$$< \dot{e}^{cr} > = a < e^{cr} > / (t - \lambda) , \tag{A-6b}$$

$$\lambda(t) = \lambda_o + \int_{t_o}^{t} \left(\frac{t - \lambda}{a}\right) \left[b \frac{\dot{\theta}}{\theta} + c \frac{< \dot{s} >}{< s >}\right] dt \tag{A-6c}$$

where A is now a material constant that does not depend on the geometry. The superscript cr indicates that Eqs.(A-6) are for creep strain. These equations are useful only if θ and $< s >$ are applied conditions. In particular, they do not handle cases of applied total strain. These latter cases correspond to stress relaxation due to the conversion of elastic strain into creep strain. Before addressing this effect, it is helpful to outline a numerical method, developed by Wilkins (Reference 3), used to relax stress by plastic flow. The extension of this method to creep flow can be derived by analogy.

The Wilkins approach involves the following steps. Compute deviatoric stress components from components of total deviatoric strain, assuming elastic theory. From Hooke's Law, the rate of change of deviatoric stress is directly proportional to the deviatoric strain rate,

$$\dot{s}_{ij}^{ee} = m \mu \dot{e}_{ij}^{tot} \tag{A-7a}$$

where m = 1 when $i \neq j$ and m = 2 when $i = j$. μ is the elastic shear modulus.

The computation of the deviatoric stress requires that Eq.(A-7a) be integrated,

$$s_{ij}^{ee}(t_n) = s_{ij}(t_o) + \dot{s}_{ij}^{ee}\Delta t \tag{A-7b}$$

where $\Delta t = t_n - t_o$, t_n is new time, and t_o is old time. The stress ellipsoids before and after the computation of the new deviatoric stress in Eq.(A-7b) are shown schematically in Figure A-4(a). These deviatoric stress components are called the equivalent-elastic deviatoric stress, $s_{ij}^{ee}(t_n)$, and are used to define a "trial" state of stress, $\sqrt{3} < s^{ee}(t_n) >$, which can be compared to the yield stress, $Y(t_n)$. If the trial state exceeds the yield surface defined by $Y(t_n)$, then all of the equivalent-elastic deviatoric stress components are reduced by the same factor,

$$\alpha = \frac{Y(t_n)}{\sqrt{3} < s^{ee}(t_n) >} \quad . \tag{A-7c}$$

Equation (A-7c) is a statement of the non-associative Prandtl-Reuss flow rule. The resulting deviatoric stress components and the corresponding plastic flow components are derived from the definition of total deviatoric strain rate as follows,

$$\dot{e}_{ij}^{tot} \equiv \dot{e}_{ij}^{e} + \dot{e}_{ij}^{p} \tag{A-8a}$$

$$\dot{e}_{ij}^{tot} = \frac{\dot{s}_{ij}^{ep}}{2\mu} + \frac{\alpha s_{ij}^{ep}(t_n)}{2\mu}$$

$$2\mu\dot{e}_{ij}^{tot} = \dot{s}_{ij}^{ep} + \alpha s_{ij}^{ep}(t_n)$$

$$\dot{s}_{ij}^{ee} = \dot{s}_{ij}^{ep} + 2\mu\dot{e}_{ij}^{p} \; . \tag{A-8b}$$

where α in the above equations is the constant of proportionality relating the rate of plastic strain to the instantaneous stress deviator in simple plastic theory.

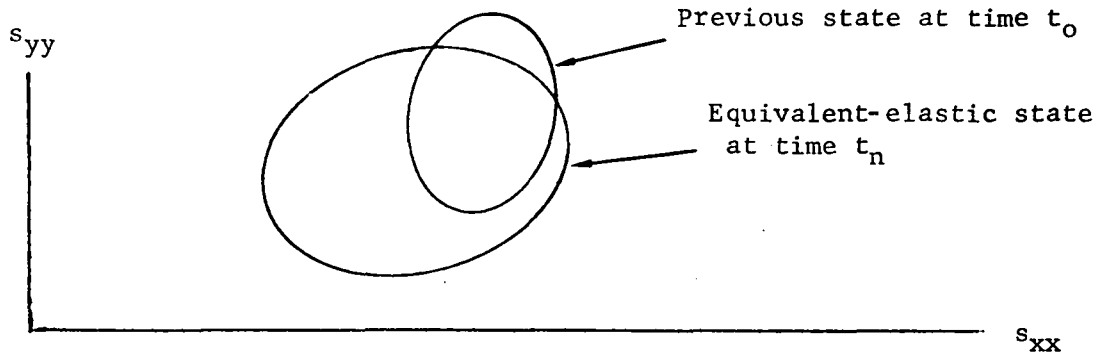

(a) Stress deviator ellipsoid before and after elastic update.

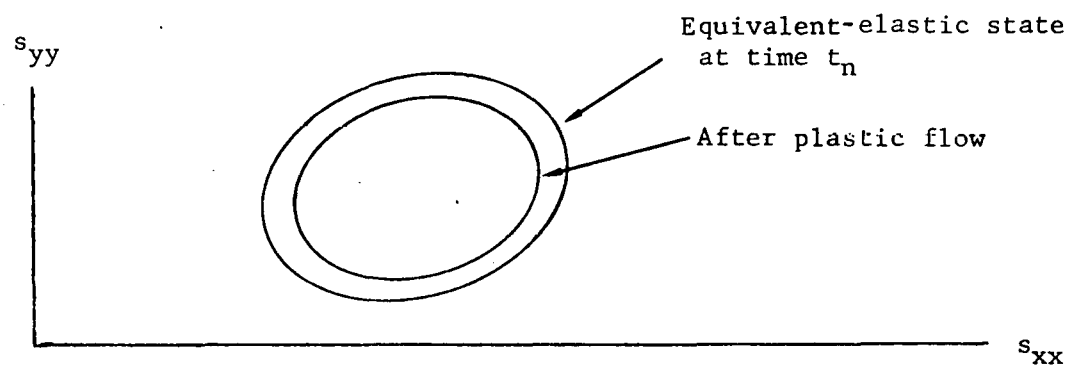

(b) Plastic adjustment by the Prandtl-Reuss assumption (not essential to the creep model).

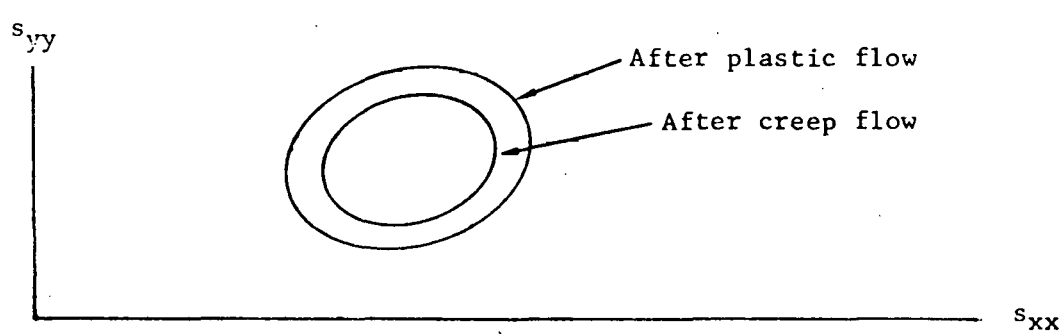

(c) Creep adjustment by the Prandtl-Reuss assumption (essential to the creep model).

Figure A-4. Update of stress deviators by elastic - plastic, and creep adjustments.

Equation (A-8b) can be rearranged as follows,

$$\dot{s}_{ij}^{ep} = \dot{s}_{ij}^{ee} - 2\mu\dot{e}_{ij}^{p} \,. \tag{A-8c}$$

In words, Eq.(A-8c) is

$$\begin{bmatrix} \text{Final} \\ \text{(elastic-plastic)} \\ \text{state of stress} \end{bmatrix} = \begin{bmatrix} \text{Trial} \\ \text{(equivalent-elastic)} \\ \text{state of stress} \end{bmatrix} - \begin{bmatrix} \text{Adjusted} \\ \text{(plastic)} \\ \text{state of stress} \end{bmatrix} \tag{A-9}$$

The elastic-plastic stress deviator, s_{ij}^{ep}, can be eliminated from Eq.(A-8c) by using Eq.(A-7c) in the following form,

$$\alpha = \frac{s_{ij}^{ep}(t_n)}{s_{ij}^{ee}(t_n)} = \frac{\dot{s}_{ij}^{ep}}{\dot{s}_{ij}^{ee}} \,. \tag{A-10}$$

Thus, Eq.(A-8c) becomes

$$\alpha\dot{s}_{ij}^{ee} = \dot{s}_{ij}^{ee} - 2\mu\dot{e}_{ij}^{p}$$

$$(1 - \alpha)\dot{s}_{ij}^{ee} = 2\mu\dot{e}_{ij}^{p}$$

$$(1 - \alpha)s_{ij}^{ee}(t_n) = 2\mu\dot{e}_{ij}^{p}\,dt \,. \tag{A-11a}$$

It can also be shown that

$$(1 - \alpha)\langle s^{ee}(t_n)\rangle = 2\mu\langle\dot{e}^{p}\rangle\,dt. \tag{A-11b}$$

The elimination of $1-\alpha$ in Eqs.(A-11a) and (A-11b) results in the equations

$$\dot{e}^p_{ij} = \langle \dot{e}^p \rangle \frac{s^{ee}_{ij}}{\langle s^{ee} \rangle} \tag{A-12}$$

which are equivalent to the assumption that plasticity shrinks the stress ellipsoid without changing its eccentricity or orientation. These remarks are illustrated in Figure A-4(b). More general models of plasticity allow for rotations and distortions of the stress ellipsoid, and these are not precluded in the discussion that follows.

If we assume that creep strain relaxes the stress ellipsoid in the same non-associative manner described above, then the corresponding creep equations are

$$\dot{e}^{cr}_{ij} = \langle \dot{e}^{cr} \rangle \frac{s^{ep}_{ij}}{\langle s^{ep} \rangle} \tag{A-13}$$

where $s^{ep}_{ij}/\langle s^{ep} \rangle$ is employed to account for general plastic response that does not necessarily obey Eqs.(A-12). This is consistent with the assumption that plastic relaxation of stresses occurs instantly, while creep relaxation requires time. Thus, the plastic adjustment is made first, followed by a creep adjustment based on the stresses that resulted from the plastic correction. Then, by direct analogy to the previous discussion [Eq.(A-8c)], the final deviatoric stresses, $s_{ij}(t_n)$, are

$$\begin{aligned} s_{ij}(t_n) &= s^{ep}_{ij}(t_n) - 2\mu \dot{e}^{cr}_{ij}\, dt \\ &= s^{ep}_{ij}(t_n) \left[1 - 2\mu \langle \dot{e}^{cr} \rangle dt / \langle s^{ep} \rangle \right] \end{aligned} \tag{A-14a}$$

$$< s(t_n) > = < s^{ep}(t_n) > - 2\mu < \dot{e}^{cr} > dt$$

$$= < s^{ep}(t_n) > \left[1 - 2\mu < \dot{e}^{cr} > dt / < s^{ep} > \right] . \qquad \text{(A-14b)}$$

The final adjustment due to creep is displayed in Figure A-4(c).

If the heat generated by creep during the stress adjustment is either (a) neglected or (b) not added until after the adjustment, then we have enough independent equations to perform the stress-strain adjustment. However, the method must be centered properly to avoid systematic errors that can occur in difference equations. The method used by SAI is described next.

Previous expressions can be used to construct the difference equations,

$$< \dot{s}(t) > \equiv \frac{< s(t_n) > - < s(t_o) >}{dt}$$

$$= \frac{< s^{ep}(t_n) > - < s(t_o) >}{dt} - 2\mu < \dot{e}^{cr} >$$

$$= \frac{< s^{ep}(t_n) > - < s(t_o) >}{dt} - 2\mu\, a A (t_n - \lambda)^{a-1} \left[\theta(t_n) \right]^b \left[< s(t_n) > \right]^c \qquad \text{(A-15)}$$

$$\dot{\lambda}(t) = \left[\lambda(t_n) - \lambda(t_o) \right] / dt$$

$$= \frac{(t_n - \lambda)}{a} \left[b\dot{\theta}(t)/\theta(t_n) + \frac{c \left\{ < s^{ep}(t_n) > - < s(t_o) > \right\}}{< s(t_n) > dt} \right]$$

$$- 2\mu\, c A (t_n - \lambda)^a \left[\theta(t_n) \right]^b \left[< s(t_n) > \right]^{c-1} . \qquad \text{(A-16)}$$

Using the following conventions,

Knowns

$$t_o = \text{old time}$$

$$t_i = \text{intermediate time } (t_o \le t_i \le t_n)$$

$$t_h = \text{half time } (t_o + t_n)/2$$

$$t_n = \text{new time}$$

$$dt = \text{full time step} = t_n - t_o$$

$$\lambda_o = \lambda(t_o)$$

$$s_o = \langle s(t_o) \rangle$$

$$s_n^{ep} = \langle s^{ep}(t_n) \rangle$$

$$R_o = \theta^b(t_o)$$

$$R_i = \theta^b(t_i)$$

$$R_n = \theta^b(t_n) \ , \quad R_h = \theta^b(t_h)$$

$$\dot{R} = (R_n - R_o)/dt$$

Unknowns

$$s_i = \langle s(t_i) \rangle$$

$$s_n = \langle s(t_n) \rangle$$

$$\lambda_i = \lambda(t_i)$$

$$\lambda_n = \lambda(t_n)$$

the difference equations can be expressed as

$$\dot{s}(t_i, \lambda_i, s_i, R_i) = \frac{s_n^{ep} - s_i}{dt} - 2\mu\, a\, \Lambda(t_i - \lambda_i)^{a-1} \; R_i s_i^c$$

$$\dot{\lambda}(t_i, \lambda_i, s_i, R_i) = \left(\frac{t_i - \lambda_i}{a}\right) \left[\frac{\dot{R}}{R_i} + \frac{c(s_n^{ep} - s_o)}{s_i dt}\right] - 2\mu\, c\, A(t_i - \lambda_i)^a \; R_i s_i^{c-1} \ .$$

These equations can be solved by a fourth-order Runge Kutta scheme as described below. The fourth-order Runge Kutta method involves four successive estimates of s and λ. The first estimates are

$$\dot{s}_1 = \dot{s}(t_o, \lambda_o, s_o, R_o)$$

$$\dot{\lambda}_1 = \dot{\lambda}(t_o, \lambda_o, s_o, R_o)$$

$$s_1(t_h) = s_o + \dot{s}_1 \, dt/2$$

$$\lambda_1(t_h) = \lambda_o + \dot{\lambda}_1 \, dt/2 \, .$$

The second estimates are

$$\dot{s}_2 = \dot{s}(t_h, \lambda_1, s_1, R_h)$$

$$\dot{\lambda}_2 = \dot{\lambda}(t_h, \lambda_1, s_1, R_h)$$

$$s_2(t_h) = s_o + \dot{s}_2 \, dt/2$$

$$\lambda_2(t_h) = \lambda_o + \dot{\lambda}_2 \, dt/2 \, .$$

The third estimates are

$$\dot{s}_3 = \dot{s}(t_h, \lambda_2, s_2, R_h)$$

$$\dot{\lambda}_3 = \dot{\lambda}(t_h, \lambda_2, s_2, R_h)$$

$$s_3(t_n) = s_o + \dot{s}_3 \, dt$$

$$\lambda_3(t_n) = \lambda_o + \dot{\lambda}_3 \, dt \, .$$

The fourth estimates are

$$\dot{s}_4 = \dot{s}(t_n, \lambda_3, s_3, R_n)$$

$$\dot{\lambda}_4 = \dot{\lambda}(t_n, \lambda_3, s_3, R_n)$$

$$s_4(t_n) = s_o + \dot{s}_4\, dt$$

$$\lambda_4(t_n) = \lambda_o + \dot{\lambda}_4\, dt\,.$$

The final estimates are

$$s_n = s_o + \frac{dt}{6}\left[\dot{s}_1 + 2\dot{s}_2 + 2\dot{s}_3 + \dot{s}_4\right]$$

$$\lambda_n = \lambda_o + \frac{dt}{6}\left[\dot{\lambda}_1 + 2\dot{\lambda}_2 + 2\dot{\lambda}_3 + \dot{\lambda}_4\right]$$

where the errors in s and λ are estimated by

$$E_s = \left|(\dot{s}_3 - \dot{s}_2)/(\dot{s}_2 - \dot{s}_1)\right| \quad \text{if} \quad \dot{s}_2 \neq \dot{s}_1$$

$$= 0 \quad \text{otherwise}$$

$$E_\lambda = \left|(\dot{\lambda}_3 - \dot{\lambda}_2)/(\dot{\lambda}_2 - \dot{\lambda}_1)\right| \quad \text{if} \quad \dot{\lambda}_2 \neq \dot{\lambda}_1$$

$$= 0 \quad \text{otherwise.}$$

The SAI model used the criterion that E_s and E_λ could not exceed 2%. If this value was exceeded using a full time step, then the calculation was repeated with sub-time steps that reduced the error to 2% or less. Though the 2% criterion is frequently used in the Runge Kutta method, it is probably more conservative than is warranted for the Project Salt Vault simulation. The trade-off of accuracy versus computer costs was not assessed.

It should be emphasized that the present SAI creep model is based on limited data, applicable to salt repository conditions, and may not be valid under different conditions. The modeling method, however, is not constrained by the particular creep law that was selected. For example, the temperature dependency, θ^b, is a satisfactory description in the limited cases of the Lomenick experiments. The dependency, $\exp(-K/\theta)$ is equally satisfactory with respect to the Lomenick experiments and probably has a larger range of validity because of its agreement with dislocation theory (Reference 4). Either form can be handled with ease by the modeling method that has been presented. If necessary, the effects of dilatancy on creep rate may also be incorporated without difficulty.

REFERENCES

1. R. L. Bradshaw and W. C. McClain, "Project Salt Vault: A Demonstration of the Disposal of High-Activity Solidified Wastes in Underground Salt Mines," ORNL-4555, Oak Ridge National Laboratory, Oak Ridge, Tennessee, 1971.

2. A. M. Starfield and W. C. McClain, "Project Salt Vault: A Case Study in Rock Mechanics," Int. J. Rock Mech. Min. Sci. and Geomech. Abstr., 10, 1973 (641-657).

3. M. L. Wilkins, "Calculation of Elastic-Plastic Flow," UCRL-7322, Rev. 1, Lawrence Radiation Laboratory, Livermore, California, January 24, 1969.

4. Hugh C. Heard, "Steady-State Flow in Polycrystalline Halite at Pressure of 2 Kilobars," Flow and Fracture of Rocks, Geophysical Monograph Series Vol. 16, 1972.

APPENDIX B
SAMPLE HEATER OUTPUT CALCULATIONS

B.1 PILLAR HEATERS

The modified pillar heater was simulated as a "line" source with a strength of 0.164 kW/m. This number was obtained by dividing the average experimental output of 3 kW by the length of the room (60 ft). Since symmetry between Rooms 2 and 3 was assumed in the simulation, there were, in essence, two modified pillar heaters in the 2D simulation, each with an output of 3 kW, but spread along the room length.

The twenty-two pillar heaters of PSV were modeled as two symmetrically placed "line" sources. The total output of 11 heaters on each side was divided by the length of the room to give 0.902 kW/m of the line source. A sample calculation is given below:

Modified heater output = 3 kW
Room length = 60 ft = 18.3 m
Modified heater output/length = 164 W/m
Pillar heater output = 1.5 kW per heater
Number of heaters on each side = 11
Total output on each side = 16.5 kW
Pillar heater output/length = 902 W/m

B.2 ARRAY HEATERS

In the experiment, the floor heaters were arranged in a circular array such that each canister was approximately 5 ft away from a neighboring canister. In order to convert this arrangement to some equivalent arrangement in 2D, these heaters were first assumed to lie along a straight line with a 5-ft spacing. Then, in a manner similar to the pillar heater output computation, the total output of the seven heaters was divided by the 30-ft

length to obtain the output of a "line" source on a per unit length basis, as shown below.

Number of array heaters = 7

Length of the straight line segment = 30 ft = 9.15 m

Total array heater output = 10.7 kW

Boosted total array heater output = 14.98 kW

Array heater output/length = 1.17 kW/m

Boosted array heater output/length = 1.64 kW/m

APPENDIX C
DYNAMIC RELAXATION

Lagrange explicit finite-difference computer programs to compute nonlinear deformation, static equilbrium, or quasi-static motion have been used by several investigators (References 1, 2, 3) with encouraging results. However, computer costs for these applications were unreasonable for engineering use. Most recently, the stress relaxation techniques (Reference 3) were modified (Reference 4) in such a way as to retain excellent numerical accuracy while reducing computer costs significantly. This method has since been interpreted (Reference 5) as a version of the dynamic relaxation method (Reference 6), which has also been applied to small-strain, elastic finite-element computer codes (Reference 7).

The equations of motion are modified as follows,

$$\Sigma F_x = m\left(\ddot{x} + \frac{\eta}{\tau}\dot{x}\right) \tag{C-1}$$

where η is a dimensional damping coefficient, $\ddot{x}$ is the acceleration resulting from the externally applied forces, F_x, and $\dot{x}$ is the velocity that results from integrating $\ddot{x}$ with critical damping applied. In terms of stress, Eq.(C-1) becomes (for a one-dimensional case)

$$\frac{\partial\sigma_{xx}}{\partial x} = \rho\left(\ddot{x} + \frac{\eta'}{\tau}\dot{x}\right), \tag{C-2}$$

where η' is $\eta/\mathcal{V}$. η (or η') is chosen to critically damp the lowest fundamental wavelength of the grid. For linear elastic problems, it is a relatively simple matter to determine the damping (or relaxation) factor from a modal analysis or a dynamic excitation without damping. Even for mildly nonlinear systems, the latter techqnique can be used. For strongly nonlinear systems, an appropriate relaxation factor is far more difficult to compute and often requires considerable judgment.

The calculational form of the dynamic relaxation equation comes from solving Eq.(C-2) for acceleration (including gravitation),

$$\ddot{x}^n = \frac{1}{\rho^n}\left(\frac{\partial\sigma_{xx}}{\partial x}\right)^n - \frac{1}{\rho^n}\frac{\eta'}{\tau}\dot{x}^n + g_x \ . \tag{C-3}$$

Integrating Eq.(C-3) with respect to time and making the following substitutions,

$$\frac{\eta'}{\rho^n} \equiv \frac{\eta}{m}$$

$$\dot{x}^n \equiv \frac{\dot{x}^{n+\frac{1}{2}} + \dot{x}^{n-\frac{1}{2}}}{2}$$

yields

$$\dot{x}^{n+\frac{1}{2}} - \dot{x}^{n-\frac{1}{2}} = \left[\frac{1}{\rho^n}\left(\frac{\partial\sigma_{xx}}{\partial x}\right)^n + g_x\right]\Delta t^n - \frac{\eta\Delta t^n}{2m\,\tau}\left(\dot{x}^{n+\frac{1}{2}} + \dot{x}^{n-\frac{1}{2}}\right) . \tag{C-4}$$

Solving Eq.(C-4) for new velocity and defining the relaxation factor, ω, to be

$$\omega \equiv \frac{\eta}{2m\tau}$$

results in

$$\dot{x}^{n+\frac{1}{2}} = \dot{x}^{n-\frac{1}{2}}\left[\frac{2}{1+\omega\Delta t^n} - 1\right] + \left(\ddot{x}^n + g_x\right)\left[\frac{\Delta t^n}{1+\omega\Delta t^n}\right] \tag{C-5}$$

where

$$\ddot{x}^n = \frac{1}{\rho^n}\left(\frac{\partial\sigma_{xx}}{\partial x}\right)^n .$$

An existing two-dimensional Lagrange explicit finite-difference computer program (Reference 8) was modified to do static calculations using the dynamic relaxation technique. A number of test calculations were made, including those that could be compared to classical solutions (References 3 and 9). The results of these computer runs showed excellent agreement with the analytic solutions and computer costs were minimal. Next, the modified code was applied to soil slope stability problems that could be compared with Bishop's method (Reference 10). Preliminary results are dramatic in that the failure region matches the limit circle derived from a factor of safety equal to one. Figures C-1 through C-4 (taken from Reference 11) show the results from a calculation of the failure of a 60° slope of cohesionless Mohr-Coulomb soil with a 25° friction angle. The problem began with the slope completely excavated, overburden specified, and gravity acting. The mesh plots show the slope failing, the vector plot shows the slope motion, and the contour plot is for vertical stress.

The results shown here indicate clearly the feasibility of the dynamic relaxation technique in adapting the explicit methods to solve static or quasi-static problems. Although a very rudimentary initial geometry and material description have been used so far, the method is completely general and can be used to calculate cases of arbitrary initial topology, complex layering, saturated or porous geologic material models, inclusion of structures such as dams or underground openings, and other features. Small-strain linear assumptions need not be used in this approach. However, nonlinear large-strain material models are only as good as the in-situ data they are supposed to represent. Time-varying boundary conditions such as sequential excavation have been tried and work well.

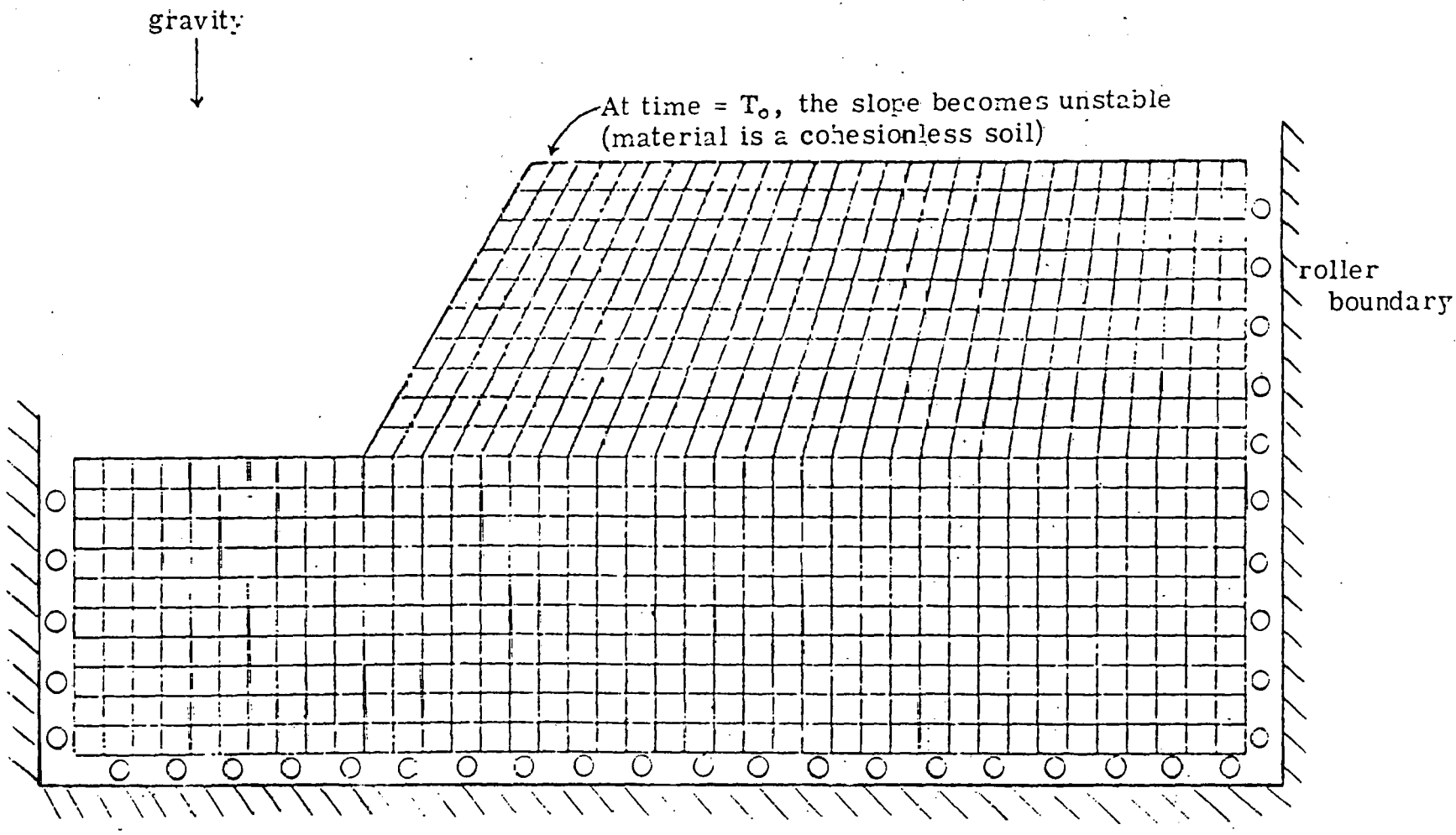

Figure C-1. Mesh plot at time = T_o, cycle 0.

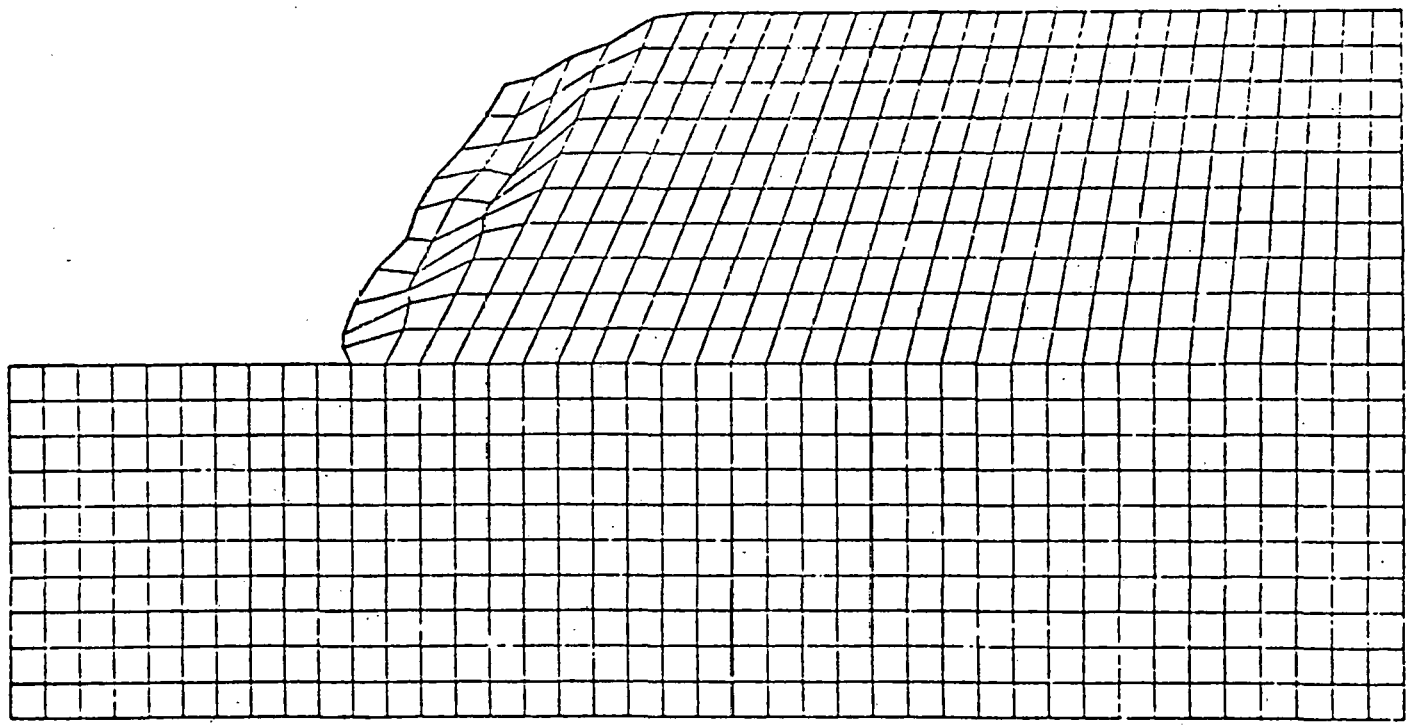

Figure C-2. Mesh plot at time = T_3, cycle 600.

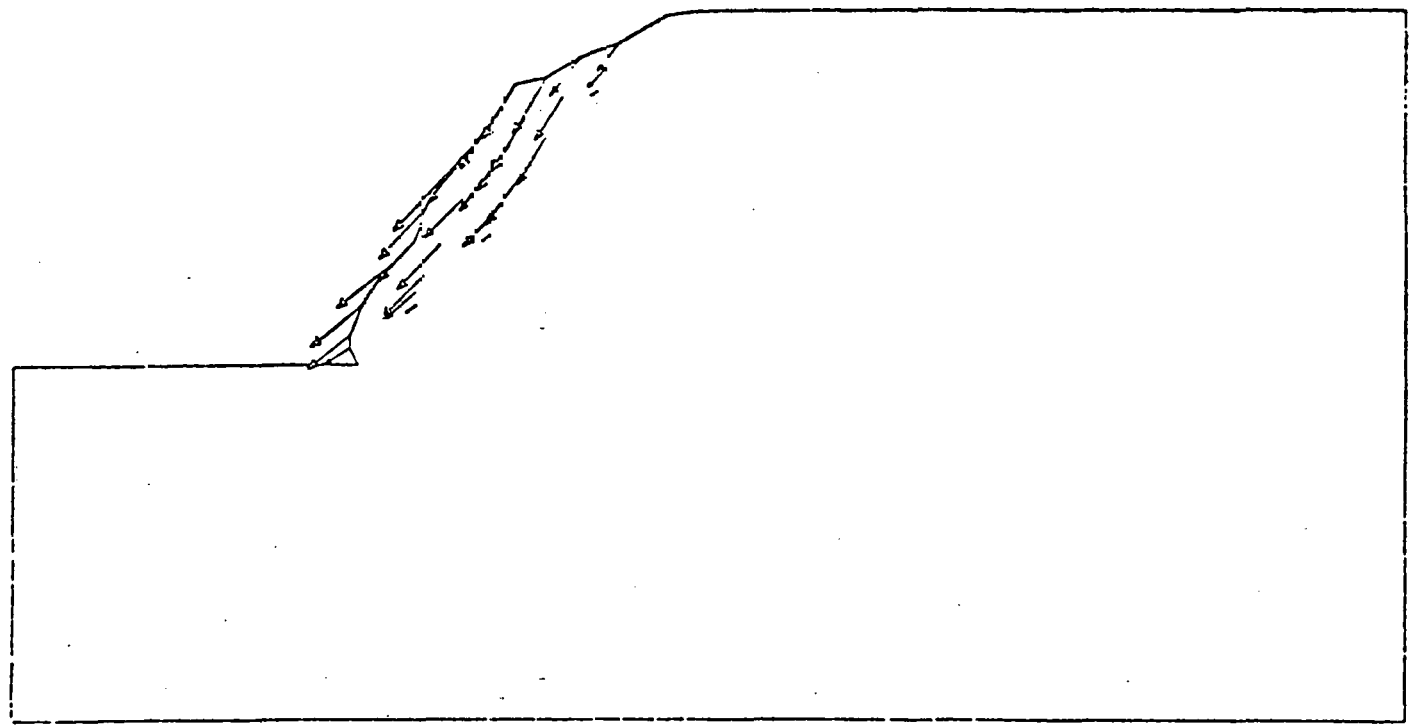

Figure C-3. Material velocity vectors at time = T_3, cycle 600.

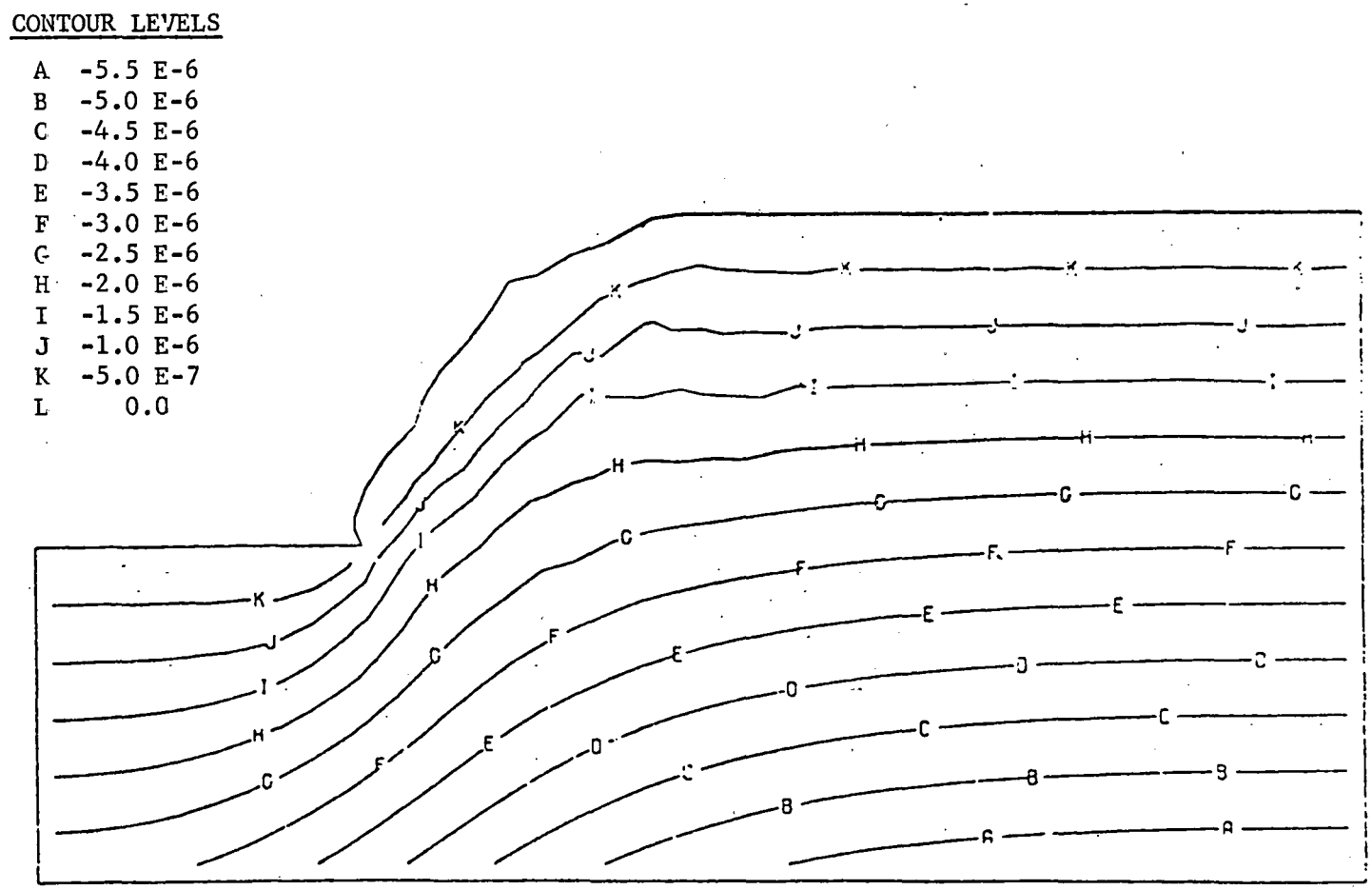

Figure C-4. Contour of vertical stresses at time = T_3, cycle 600.

APPENDIX C

REFERENCES

1. G. Maenchen and S. Sack, "The TENSOR Code," UCRL-7316, Lawrence Radiation Laboratory, Livermore, California, April 9, 1963.

2. Mark L. Wilkins, private communication, 1973.

3. D. J. Andrews and Steven L. Hancock, "A Relaxation Method for Solving Nonlinear Stress Equilibrium Problems," J. Comp. Phys., 12 2, June 1973.

4. Steven L. Hancock, "Numerical Convergence to Mechanical Equilibrium with a Velocity Damping Method and Its Interpretation as Simultaneous Overrelaxation," TCAM 73-8, Physics International Company, San Leandro, California, July 1973.

5. Steven L. Hancock, private communication, 1973.

6. Joseph Reuben Harry Otter, Alfred Carlo Cassell, and Roger Edwin Hobbs, "Dynamic Relaxation," Proc. Inst. Civ. Engrs., 1966, 35 (Dec.) 633-656, and 37 (Aug.) 723-750.

7. A. C. Cassell, "Shells of Revolution Under Arbitrary Loading and the Use of Fictitious Densities in Dynamic Relaxation," Proc. Inst. Civ. Engrs., 1970, 45 (Jan.) 65-78, and 47 (Nov.) 389-395.

8. Ronald Hofmann, "PISCES Manuals," Physics International Company, San Leandro, California, 1974.

9. Steven L. Hancock and Raymond Hsu, "A 1DL Quasi-Static Test Calculation: A Plastic-Elastic Spherical Shell," TCAM 73-9, Physics International Company, San Leandro, California, June 1973.

10. A. W. Bishop, "The Use of the Slip Circle in the Stability Analyses of Slopes," Geotechnique, 5 1, March 1955.

11. R. D. Hammett, "A Study of the Behaviour of Discontinuous Rock Masses," Thesis for the Degree of Doctor of Philosophy, Department of Engineering, James Cook University of North Queensland, Australia, December 1974.